Mechanical characterization and modeling of the deformation and failure of the highly cross-linked RTM6 epoxy resin

X. P. Morelle[a], J. Chevalier[a], C. Bailly[b], T. Pardoen[a], F. Lani[a,*]

[a]*Institute of Mechanics, Materials and Civil Engineering, Université catholique de Louvain, Place Sainte-Barbe, n°2, L5.02.02, 1348 – Louvain-la-Neuve, Belgium.*
[b]*Institute of Condensed Matter and Nanosciences, Université catholique de Louvain, Croix du Sud, n°1, L7.04.02, 1348 – Louvain-la-Neuve, Belgium.*

Abstract

The non-linear deformation and fracture of the RTM6 resin is characterized as a function of strain rate and temperature under various loading conditions involving uniaxial tension, notched tension, uniaxial compression, torsion and shear. The RTM6 resin is heavily used in the aeronautic industry as the matrix for advanced composites and is representative of this class of highly-crosslinked thermoset systems. A Drucker-Prager pressure-dependent constitutive model is built with a specific hardening law inspired from finite strain elastic-viscoplastic models for thermoplastics. The parameters of the hardening law depend on strain-rate and temperature. The pressure-dependence and hardening law, as well as four different failure criteria are identified against the experimental results. The constitutive model and a plastic strain at failure criterion are readily introduced in the standard version of Abaqus, without the need for coding user subroutines. The model is successfully assessed against results of progressive failure in V-notched beam shear test. Besides, detailed fractography analysis provide insight into the competition between shear yielding and maximum principal stress driven brittle failure.

Keywords: RTM6, highly crosslinked epoxy resin, elasto-viscoplasticity, fracture criterion, constitutive modeling, aerospace composite

1. Introduction

Multi-scale mechanical modeling approaches require reliable constitutive models and failure criteria for the constituents as well as accurate experimental data for parameter identification in order to reach the highest possible predictive capability, for stress analyses, in the frame of virtual testing of complex composite systems, or for the purpose of designing new hybrid materials [Canal et al., 2012]. High performance adhesives and polymer composites constitute two important families of hybrid systems, among which many rely on widespread thermoset epoxy resins. Two main classes of epoxies have been studied in the literature, from both mechanical characterization and modeling standpoints:

*Corresponding author.
Email address: frederic.lani@uclouvain.be (F. Lani)

- The largest part of the literature focuses on moderately crosslinked ductile epoxies, based on a difunctional precursor such a diglicidyl ether of bisphenol A or DGEBA and tetrafunctional, mostly amine, hardener. They are very much used, blended with other constituents, for structural adhesive applications.
- A more limited part of the literature is dedicated to the characterization and modeling of the deformation and failure behavior of highly crosslinked epoxies such as RTM6, based on tetrafunctional precursor and (amine) hardener.

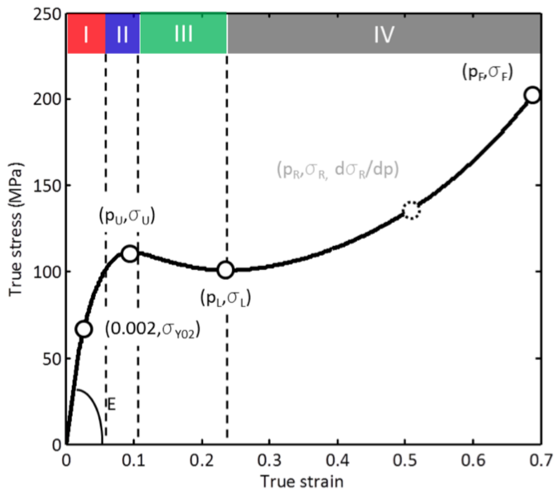

Figure 1: The four deformations stages of an amorphous glassy polymer: stage I - elastic-viscoelastic deformation; stage II - onset of plastic flow; stage III - strain softening; stage IV - strain-hardening.

The stress-strain response of these epoxies is similar to that of amorphous glassy thermoplastics. Depending on the loading conditions (strain rate, temperature, stress triaxiality), amorphous glassy polymers hence the RTM6 exhibit four different deformation stages, as illustrated in Fig.1.

First, the response is elastic-viscoelastic (stage I), where the deformation is mainly due to secondary intermolecular interactions [Meijer and Govaert, 2005]. As the viscoelastic component increases with time, the curve slowly and slightly departs from linearity. This small strain region can be significantly affected by strain-rate and temperature.

Second, the yield process starts and plastic flow sets in (stage II), as the activation barrier to main chain segmental motion is overcome. That yield transient is very much affected by strain-rate, temperature and hydrostatic pressure, see e.g. Eyring's theory [Eyring, 1936; Ree and Eyring, 1955] of transition of state, or Argon's thermally-mechanically activated double-kink mechanism [Argon, 1973; Argon and Bessonov, 1977], as well as by the thermo-mechanical history of the polymer, related to physical aging (increase) or mechanical rejuvenation (decrease) [Govaert et al., 2000; Klompen et al., 2005; Meijer and Govaert, 2005; Tervoort et al., 1996].

Third, and closely following the yield point, softening occurs due to large inter-molecular movement (stage III). The origin of softening is still subject to debate. When strain-localization / macroscopic shear banding is allowed to occur due to the specimen geometry and boundary conditions, softening can obviously take place; if re-hardening takes places, shear bands thicken and the sample re-hardens as a whole, if not the specimen fails. In other circumstances, where no shear banding is extrinsically triggered, it is now admitted that micro-shear banding can occur as a true material feature. The kinetics of initiation, growth and coalescence of shearing zones determine the yield drop and softening rate [Hasan and Boyce, 1995; Homer and Schuh, 2009; Marano and Rink, 2001; Oleynik, 1989; Quinson et al., 1996; Sindt et al., 1996]. Both the onset of yielding and the softening stage are believed to be associated with free-volume rearrangement [Hasan et al., 1993; Jatin et al., 2013; Struik, 1991].

Fourth and finally, rubber-like elastic response of the network starts to prevail at large strains through chain reorientation [G'Sell and Gopez, 1985; Sindt et al., 1996] balanced by the fact that only limited stretch ratios can be achieved in highly cross-linked thermosets. This phenomenon is called strain re-hardening (stage IV) and results from the entropic resistance to the alignment of the molecular network. It is thus most of the time deemed independent of prior thermo-mechanical history but can be much affected by the cross-links density [Senden et al., 2010], and, in a lesser extent by temperature and rate [Govaert et al., 2008].

This behavior has been largely reported for thermoplastic polymers (e.g. PMMA and PC) loaded in compression, shear or tension up to very large fracture strains. Hence, there is a huge literature on the joint thermal-mechanical characterization and finite strain elastic-viscoplastic constitutive modeling of the strain-rate, temperature and pressure sensitive response of glassy polymers up to very large deformations [Boyce et al., 1988; Haward and Thackray, 1968; Tervoort and Govaert, 1998].

Large fracture strains are also attained in moderately and highly crosslinked epoxies loaded in uniaxial compression. Unlike RTM6 which fail prematurely for any other loading than compression, moderately crosslinked epoxies can still exhibit some ductility in shear and tension. However, while the macroscopic response of RTM6 loaded in compression exhibits many similarities with glassy thermoplastics loaded in tension or compression, which suggest that the fundamental origins of plastic flow, softening and re-hardening are identical in both types of polymers [Yamini and Young, 1980]. However, no similarities in terms of progressive damage mechanisms (e.g. crazing) have ever been reported [Asp et al., 1996].

Most researches dealing with the characterization and modeling of thermoset epoxy resins cover only part of the triangle "strain-rate - temperature - pressure" sensitivity of the relationship between stress and strain. Besides, some works are dealing only with the characterization of the strain-rate, temperature and pressure dependence of the peak yield or of the onset of yielding (e.g. [Gómez-del Río and Rodríguez, 2012; Sindt et al., 1996]), while others cover the full range of deformation, including softening and re-hardening when these stages are actually observed [Poulain et al., 2014, 2013]. Moreover, most studies focusing on the non-linear behavior of the resin do not address the problem of final failure, and vice-et-versa. An interesting common point to several researches is the characterization and modeling of the competition between shear yielding related with fundamental intrinsic shear deformation mechanisms [Hasan and Boyce, 1995; Sindt et al., 1996], and micro-cavitation occurring mainly in the presence of positive hydrostatic stress and/or positive maximum principal stress [Asp et al., 1996; Fiedler et al., 2001, 2005; Hobbiebrunken and Fiedler, 2007; Liang and Liechti, 1996].

However, very few studies are dedicated to the detailed modeling of the deformation and failure of the structural RTM6 epoxy resin itself. Nevertheless, it is worth mentioning the work by Gerlach et al. [Gerlach et al., 2008] in which the RTM6 was tested at room temperature both in compression and tension under impact loading, covering about 6 decades of strain rates. Their results showed the bilinear dependence of the peak-yield stress on the log of the strain rate, with a slope transition between 'quasi-static' and impact loadings. The experiment results revealed also the strong dependence of the apparent Young's modulus on the strain rate, with again a transition between ‘quasi-static’ and impact regimes. This strongly rate dependent behaviour of RTM6 was modeled (up to the peak yield) using the Goldberg elastic-viscoplastic model [Goldberg et al., 2003], also accounting for effects of the hydrostatic pressure. In [Fiedler et al., 2005], Hobbiebruken et al. characterized the RTM6 epoxy resin in uniaxial tension at different temperatures and and at a single, low, strain-rate. A strong dependence of the yield stress, failure stress and failure strain on the temperature was found. Shear yielding was found to occur at high temperatures while a premature brittle behavior was observed at lower temperatures. A Von Mises yield surface and associated flow rule were used, with simple rate independent hardening law fitted to the experimental curves at the different temperatures. One of the salient facts of their study was the strong effect of the resin non-linearity on the resulting composite thermal residual stress.

There is a growing demand for better mechanical characterization of structural epoxies coming from experts in modeling as well as from materials designers and engineers dealing with the stress analysis of composites. Therefore, a large characterization and modeling effort has been carried out in this work on the highly crosslinked RTM6 structural epoxy resin by Hexcel corp. The first aim of this research is to lead to a better understanding of the competition between thermally as well as stress activated shear-dominated (visco-)plastic deformation and micro-cavitation-induced brittle failure. The second outcome of this study is to provide the community with a carefully assessed strain-rate, temperature and pressure sensitive constitutive model and a pressure-dependent failure criterion (the latter at room temperature only) for the RTM6 resin involving the set of identified parameters. The models are ready for use ’as is’ in most commercial general purpose finite element software, and in particular in Abaqus [V6.12]. On the one hand, the proposed constitutive model lacks the generic character of finite strain elastic-viscoplastic constitutive models developed and identified for instance by [Poulain et al., 2014] on epoxy, [Anand et al., 2009; Anand and Gurtin, 2003; Boyce et al., 1988; Gearing and Anand, 2004; Hasan and Boyce, 1995; Tervoort and Govaert, 1998] on PC or PMMA. On the other hand, it shows greater applicability and ease of use for engineers and researchers, avoiding the need for user material subroutines.

The paper is organized as follows. Section 2 presents the materials and manufacturing conditions of the test samples; section 3 describes all the mechanical tests. Section 4 presents the experimental results (compression, tension, torsion) that will be used for the identification and preliminary assessment of the constitutive model, as well as a detailed fracture analysis after the different mechanical tests. Section 5 explains the ingredients of the non-linear constitutive model, its identification against experimental results and its validation. Section 6 presents a selection of failure criteria, their identification and validation. Section 7 contains a first critical full assessment of the deformation and failure model by comparison of FE simulation results and experimental data for the V-notch beam (Iosipescu) test. Final conclusions and future work are described in section 8.

2. Materials

Hexflow RTM6, supplied by Hexcel, is a mono-component epoxy resin specifically developed to fulfill the requirements of the aeronautics and space industries regarding advanced resin transfer moulding processes. This amine-cured highly cross-linked thermoset is composed of a premixed system [Dumont, 2013; Kiuna et al., 2002] of a tetra-functional epoxide precursor (Tetra-glycidyl methylene dianiline or TGMDA) and a blend of two di-amine hardeners (MDEA and MMIPA). RTM6 shows good process-ability through a convenient injection window for industrial use.

After curing, RTM6 has a glass transition temperature (T_g) around $220°C$, determined by differential scanning calorimetry (DSC) and dynamic mechanical analysis testing (DMA), thus providing high stiffness ($E = 3\ [GPa]$ at room temperature) and good thermal stability properties with a service temperature ranging from $-60°C$ to $180°C$.

A specific cure cycle was developed in order to manufacture thick resin slabs and cylinders with a minimum of 95% degree of conversion while avoiding resin degradation in the core of the specimen. Hence, a large variety of test specimens was manufactured with reproducible thermal-mechanical history and consistent thermal-mechanical properties. The uncured resin mixture is first poured in open release-agent coated molds and degassed for $75\,min$ at $90°C$ under vacuum. Then, in an air-circulated oven, the applied curing cycle uses a $2°C/min$ heating ramp to $130°C$, $3\,h$ dwell at $130°C$, $2°C/min$ heating to $180°C$ and finally $3\,h$ of post-curing at $180°C$ to achieve the expected degree of conversion. The reproducibility of the materials condition after curing was verified in several locations of the specimens obtained in the different molds by measuring the residual reaction enthalpy with alternating DSC, confirming that a degree of cure between 95% and 97% could be achieved.

3. Mechanical testing

3.1. Samples and methods

Cylindrical resin slabs were machined into small cylindrical specimens for uniaxial compression tests and into cylindrical dog bone specimens for the uniaxial tensile tests. Notched tensile specimens were prepared by machining the cylindrical dog bone specimen with different notch radii. Larger cylindrical slabs were produced in order to machine hollow torsion specimen. V-notched beam specimens were obtained from rectangular slabs. The different specimens are shown in Fig.2, the dimensions and standards that have been followed are provided in Table 1.

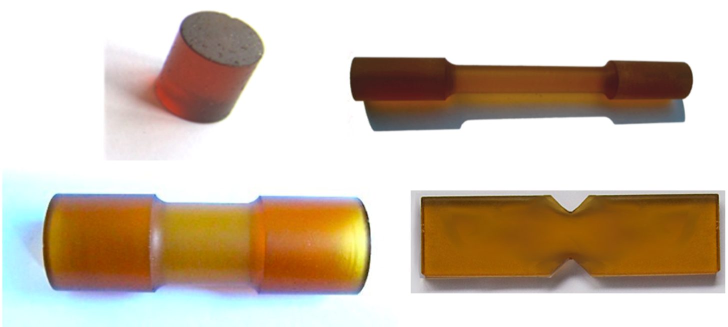

Figure 2: Bulk resin samples for mechanical testing. Top-left: cylindrical samples for uniaxial compression testing; top-right: dog-bone specimen for uniaxial tension (note: notched specimen were also manufactured); bottom-left: hollow tubular sample for torsion testing; bottom-right: V-notch beam specimen for model assessment.

The compression, tension, notched tension and V-notch beam tests were carried out on a screw-driven universal testing machine (Zwick-Roell with an external load cell of 250 [kN]).

Type of test	International standard	Length [mm]	Diameter [mm]	Notch radius [mm]
Uniaxial compression	ASTM D695	12	12	-
Uniaxial compression testing sensitivity to friction	ISO604	6	12	-
Uniaxial tension (Small specimen)	ASTM D638	36 (gauge length)	6	-
Uniaxial tension (Large specimen)	ASTM D638	50 (gauge length)	9	-
Notched tension	-	50 (gauge length)	9 (original diameter) and 4 (section diameter in the notch)	1, 3, 5
Torsion	-	12 (gauge length)	16 (outer diameter) and 12 (inner diameter)	-
Iosipescu	ASTM D5379	80 (length) and 20 (height)	4 (thickness)	v-notch of 90° opening angle with end-radius of 1.5

Table 1: Summary of dimensions and corresponding inspirational standards for all tested specimens.

The torsion tests were performed on a hydraulic axial-torsion machine MTS 000337/002280 Type 319-25C with 250 [kN] load cell. The tests were performed in a conditioned room with controlled temperature ($23°C \ \ +/-3°C$) and relative humidity ($50\% +/-10\%$). The target temperature and relative humidity are selected according to ASTM D3479.

The compression tests were performed either at constant true strain rate (CSR) or at constant crosshead displacement rate (CCDR) covering 4 decades of strain rates (between $10^{-4}\,s^{-1}$ and $0.1\,s^{-1}$ for the CSR tests and between $\approx\ 1.65\,10^{-4}\,s^{-1}$ and $\approx\ 0.165\,s^{-1}$ for the CCDR tests). Teflon strips were used as solid lubricant between the compression platens and the samples in order to minimize the barreling effect. Compared with any other liquid lubricant (e.g. grease oil), Teflon really allowed avoiding the development of specimen barreling. All the compression tests were performed at three different temperatures: room temperature $\approx 20°C$ ($293\,K$), $100°C$ ($373\,K$) and $150°C$ ($423\,K$). The axial strain was obtained from the crosshead displacement, corrected in order to account for the so-called machine compliance. The absence of friction and shear-banding or localization allows the use of the experimental results for the construction of reliable true-stress / true-strain curves. At room temperature, on a subset of compression samples, the radial strain is measured either by using a LVDT or by analysis of images taken from videos of the tests, allowing for the estimation of the plastic Poisson ratio.

The behavior in tension has been characterized either at a constant true strain rate of $10^{-3}\ s^{-1}$ (CSR tests) or at a constant crosshead displacement rate of $1\,mm/min$ (CCDR tests). The CSR tests were performed at room temperature only, while the CCDR tests were performed at room temperature $\approx 20°C$ ($293\,K$), $100°C$ ($373\,K$) and $150°C$ ($423\,K$). The axial strain was measured using contact extensometers in the gauge length. Above $100°C$, localization occurred in a subset of specimen which would ideally require the use of digital image correlation for adequate post processing of the strains in the gauge length. However the option taken was to exclude these specimens out of the database for the identification of the constitutive model.

The response of the notched tensile specimens, with the 3 different radii, has been characterized at a constant crosshead displacement rate of 1mm/min, at room temperature only. The radial displacement in the notch was measured using a strictometer (LVDT).

The torsion tests were conducted at room temperature and under a single rotation rate of $7°/min$. Three-element 45° rectangular rosette strain gauges were bonded onto the torsion specimen surface to measure the shear strain in the gauge section. Such strain gauges cannot operate above 10-15% of strain, therefore a correlation was used between the measured value of shear strain (with the strain gauge) and the applied rotation angle in order to get a reliable estimation of larger shear strain. The large majority of the tests failed before shear-banding could be observed, making these tests eligible for the identification of the parameters of a constitutive model.

The V-notched beam tests were conducted at room temperature only, with a single crosshead displacement rate of $1\,mm/min$. Back to back bidirectional strain gauges were bonded onto the specimen surface between the notch roots at 45° with respect to the horizontal axis, in order to measure the local maximum and minimum principal strains, translated into shear strain.

A minimum of three valid test results are available for each condition, except for the constant crosshead displacement rate compression tests, where, beside the $1\,mm/min$ case where six valid tests results are available, only one or two samples could be tested. The constant true strain rate tests were performed with a single batch of resin. Samples taken from several batches were used to conduct the other tests. Note that the variability within a batch is very limited (except for what concerns the failure stress and strain, see below) while significant batch to batch variability can be observed for most of the measured mechanical properties.

3.2. Note on the determination of a representative strain rate

None of the constant true strain rate or the constant crosshead displacement rate test conditions lead to a constant true plastic strain rate over the entire deformation range. However, when assessing the non-linear deformation behavior of materials, comparison between hardening curves is meaningful only when similar equivalent plastic strain evolutions are encountered in the different tests, e.g. the authors of [Liang and Liechti, 1996] invoke differences of strain-rate between different tests to explain certain inconsistencies of hierarchy of yield strengths (e.g. peak yield) between different types of tests. Therefore, two measures of the average equivalent plastic strain rate are used which allow to rigorously compare the strain-rate sensitivity of the materials: a 'low-range' or small strain average (plastic strain below 0.07) and a 'full-range' or large strain average (up to 0.7). When premature failure of the specimen is observed before the plastic strain is reaching 0.07, the plastic strain evolution is extrapolated up to 0.07 in such a way as to mimic the response of a compression or torsion test, providing an estimation of the low-range plastic strain rate average. Besides, thorough examination of the compression tests showed that the full-range average is about $3/2$ of the low-range average, providing also an estimation of the full-range average plastic strain rate for specimen that do not exhibit large ductility.

Here is a summary of how these plastic strain rate averages are used:

- when comparing compression tests between them, the full-range plastic strain rate average is available and used;
- when comparing tensile tests between them, the low-range plastic strain rate average is used, either based on the available data or estimated by extrapolation up to 0.07;
- when comparing different types of tests, the full-range plastic strain rate average is used, either based on available data (for compression tests) or on estimations by extrapolation.

4. Experimental results

The mechanical response of the RTM6 will be presented under the form of 'true stress - true strain' or 'true stress - true plastic strain' curves. These curves will be carefully analyzed in terms of remarkable features and/or points as illustrated in Fig.1 :

- the elastic modulus E
- the yield stress at a 0.2% plastic strain $\sigma_{Y_{0.2\%}}$
- the peak yield stress and plastic strain at peak yield p_U
- the lower yield stress σ_L
- the failure stress and plastic strain at failure p_F.

The other data such as the plastic strain at the lower yield level p_L, or the incremental strain-hardening coefficient at an intermediate plastic strain p_R in the fourth stage of deformation will not be addressed in details although they can be used to help identifying the hardening law.

4.1. *Strain-rate, temperature and pressure dependence*

The variation of the elastic modulus in compression as a function of the plastic strain rates are shown in Fig.3 a) and b) for various temperatures. The temperature dependence of the elastic modulus in tension is shown in Fig.3. Note that the compressive and tensile CSR tests were made with the same batch of resin while the CCDR compressive and tensile tests were performed with samples coming from different batches, but without samples coming from the 'CSR batch'. As a result, batch to batch variability of modulus of 10 to 15% can be observed, whatever the temperature.

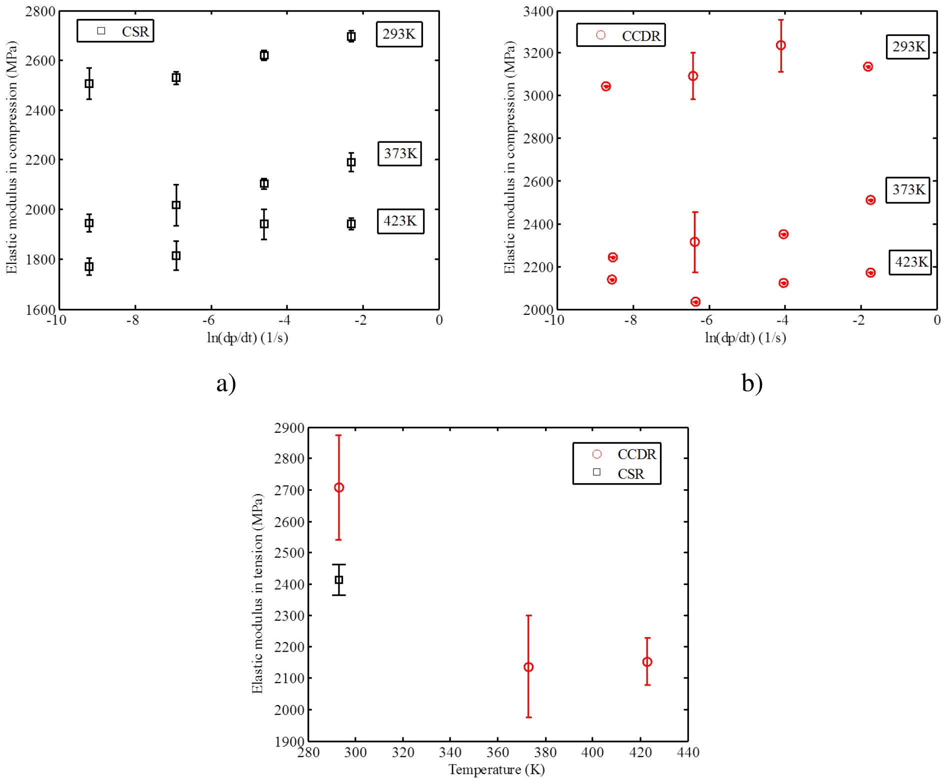

a) b) c)

Figure 3: Measured temperature and strain-rate dependence of the Young's modulus in a) compression with Constant Strain Rate (CSR) tests on a single batch, b) compression with Constant Crosshead Displacement Rate (CCDR) tests and multiple batches, c) tension under both CSR (single-batch) and CCDR (multi-batch) test conditions.

Compression tests results at constant true strain rate and constant crosshead displacement rate are shown in Fig.4 a) and b), respectively. Tensile test results at constant crosshead displacement rate are shown in Fig.4 c). Not all but only representative true stress- true strain curves are shown in these figures. The tensile curves obtained at constant true strain rate are not shown as sliding within the grips was observed; although the tests had to be invalidated, the measured elastic moduli and corrected failures stress were consistent and thus kept in the database. In Fig.4 c) the low and full-range averages of the true plastic strain rate are shown for information.

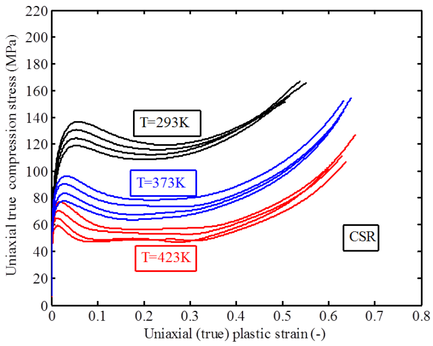

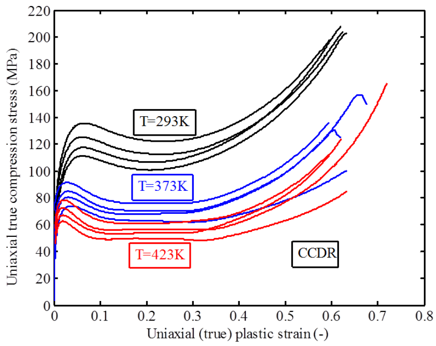

a) b)

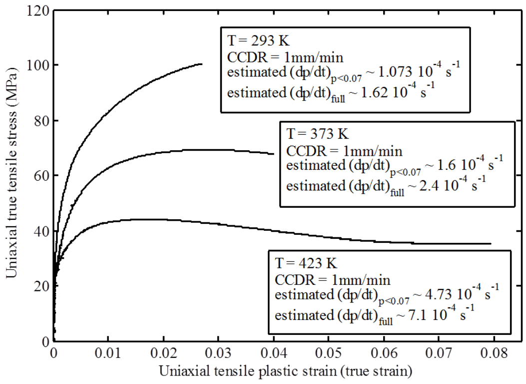

c)

Figure 4: Representative uniaxial true stress versus uniaxial true plastic strain curves for three temperatures ($293K$, $373K$, $423K$) in a) compression with constant true strain rate tests (from 10^{-4} to 10^{-1} $1/s$) and a single batch, b) compression with constant crosshead displacement rate (from 0.1 to $100\,mm/min$) and multiple batches, c) tension with constant crosshead displacement rate (the estimated average plastic strain rates are also provided). Note: tensile tests conducted at constant strain rate were partially invalidated due to sliding in the grips and are not shown (only the elastic modulus & corrected final failure stress were kept in the database).

The comparison of Fig.4 a) and b) reveals that there is a $50\,[MPa]$ and a 0.1 drop of failure stress and plastic strain at failure, respectively, for the constant true strain rate tests conducted at room temperature. No other explanation than the batch/operator variability can be given to explain this difference. The Poisson ratio the plastic Poisson ratio were measured on a subset of uniaxial compression tests, giving average values equal to ≈ 0.34 and ≈ 0.5 (minimum value: 0.48, maximum 0.51), respectively. The latter suggests that plastic deformation is isochoric.

Fig.5 illustrates the strain-rate and temperature dependence of the characteristic strength values defined in Figure 1 for the uniaxial compression tests. Batch to batch variability of up to 10% can be observed for the 0.2%yield, the peak yield and the lower yield stresses, whatever the strain-rate and temperature. In Fig.5 a), b) and c), the stress varies linearly with the logarithm of the true plastic strain rate. The range of strain-rates addressed in this paper does not allow to observe a transition from quasi-static to dynamic regimes such as observed by Gerlach et al. in

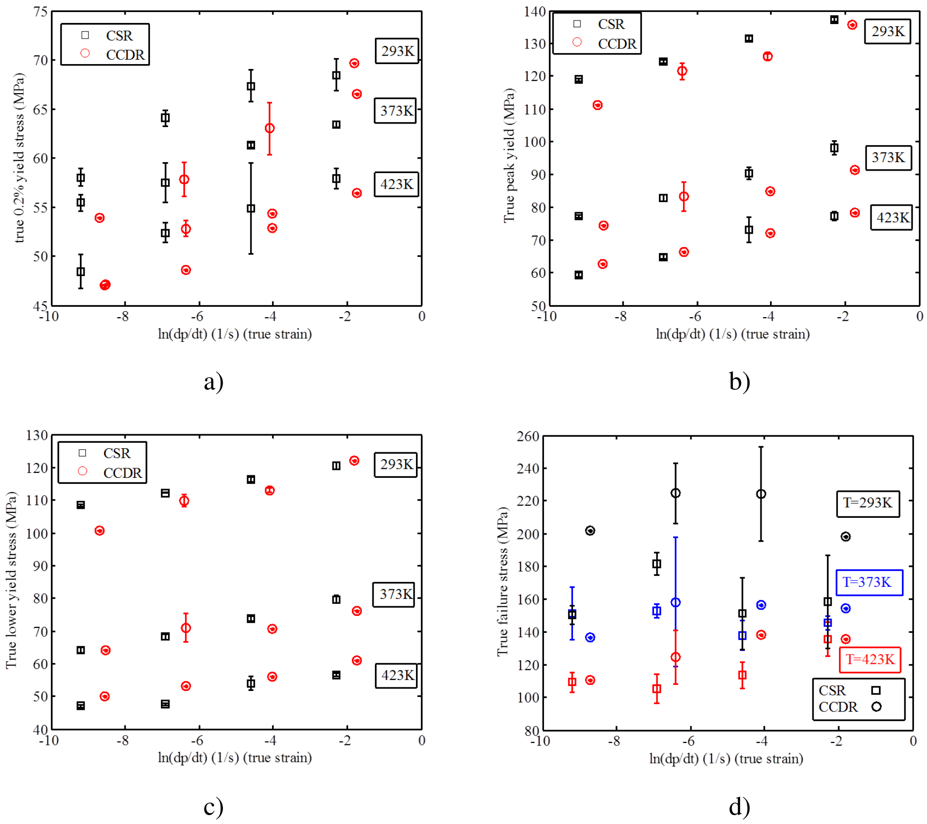

Figure 5: Evolution of the remarkable true stress values: a) 0.2% plastic strain yield stress, b) peak yield stress, c) lower yield stress, d) failure stress.

[Gerlach et al., 2008]. Fig.5 d) suggests that the failure stress in compression is rather insensitive to plastic strain rate, and also shows, in general; a large variability.

To complement the analysis of the strain-rate and temperature dependence of the uniaxial compression stress-strain curve, Fig.6 a) and b) also show the evolution of the plastic strain at peak yield and plastic strain at failure, respectively. Both look rather insensitive to strain-rate, and, when considering the CSR tensile tests at RT as outliers, the plastic strain at failure is almost independent of temperature.

A comparison of representative Von Mises stress - effective plastic strain curves determined based on the compression, tension and torsion tests is shown in Fig.7, where the estimated average plastic strain rates are also indicated. In this figure, the effect of an error in the estimation of the average plastic strain rate on the stress-strain curve is shown, anticipatively using the constitutive model presented in the next sections. In particular, it highlights the fact that a correct estimation of the plastic strain rate is important when dealing with the identification of the asymmetry of yielding between tension and compression.

Finally, the pressure and temperature dependence of the Von Mises stress and effective plastic strain at failure are shown in Fig.8 a) to c) In these figures, the x-axis is the stress triaxiality

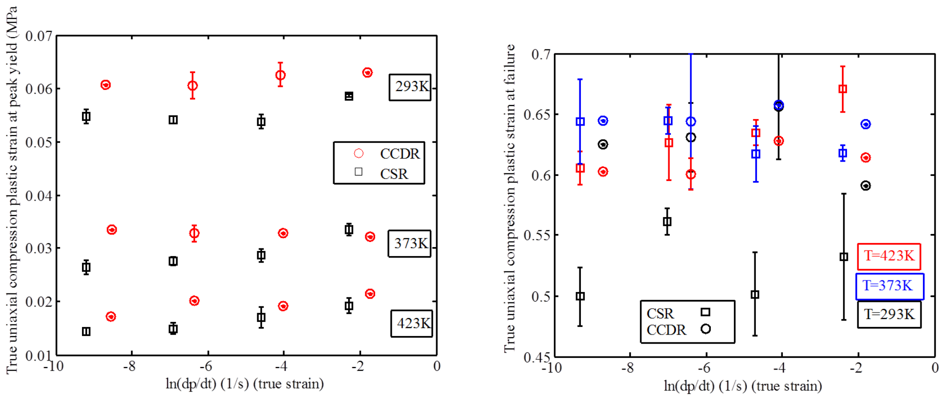

a) b)

Figure 6: Evolution of the remarkable true plastic strain values: a) true uniaxial plastic strain at peak yield, b) true uniaxial plastic strain at failure.

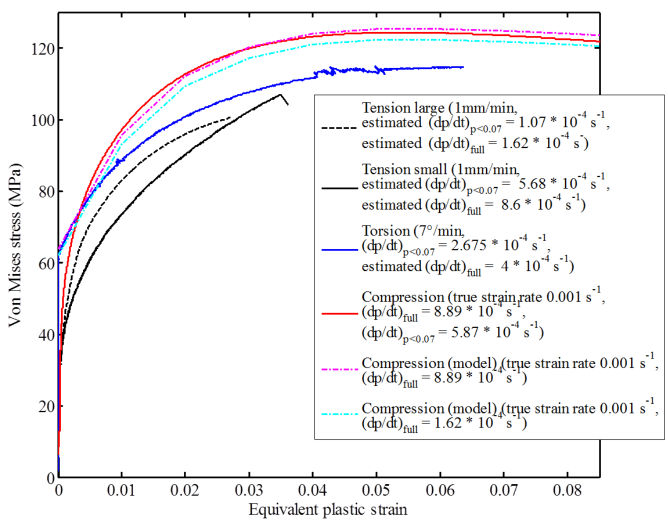

Figure 7: Representative 'Effective (Von Mises) stress versus Equivalent plastic strain curve' for the different types of loadings (compression, tension, torsion). Also shown: the estimations of the 'low-range' and 'full-range' effective plastic strain rates.

computed as

$$\mathbf{t} = \frac{\sigma_{mm}}{3\sigma_e} \tag{1}$$

where σ_e is the Von Mises stress and $\frac{\sigma_{mm}}{3}$ is the hydrostatic stress. The plotted stress and plastic strain values are actually averaged over all the strain-rates.

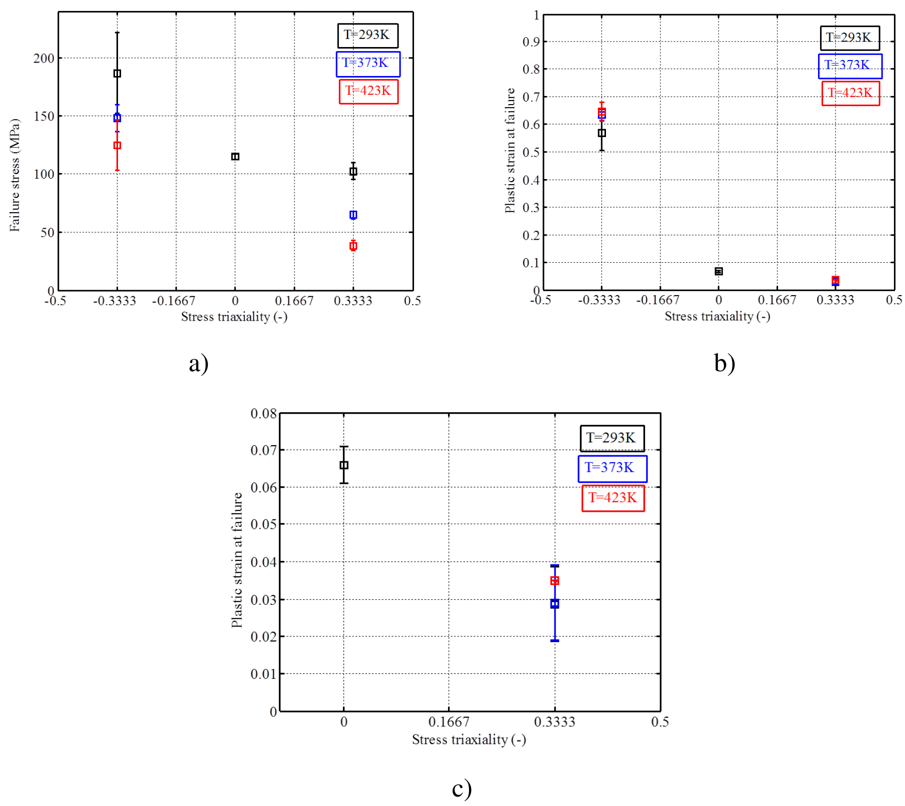

Figure 8: a) Variation fot the effective failure stress as a function of stress triaxiality (tension = 1/3, torsion=0, compression=-1/3), b) Variation of the effective plastic strain at failure as a function of stress triaxiality, c) zoom on the effective plastic strain at failure for positive triaxialities.

4.2. Fractographic analysis

The tensile and notched tensile specimens failed in a brittle manner after limited plastic deformation, with very similar fracture surfaces. Fig.9.a shows SEM micrographs and Fig.9.b shows a schematic representation of the typical pattern observed on these surfaces. First, the fracture process is triggered by the nucleation of a crack at a defect in the gauge section. The crack initiation spot can usually be readily located on the surfaces (see micrograph A in Fig.9.a). The evolution of the fracture surface pattern agrees with previous observations of the fracture surfaces of epoxy resins [Fiedler et al., 2001; **?**; **?**; **?**] or even of other glassy polymers such as PMMA [**??**]. Indeed, as described in [**?**], the fracture of thermoset polymers follows several distinct stages which are depicted in the central scheme of Fig.9.b. After the initiation of the crack at a defect, a smooth and featureless region, often referred to as mirror-like, corresponds to the slow propagation of the crack. A textured microflow, such as described by Greenhalgh [**?**], is also often observed in this first region. Then, the acceleration of the crack leads to a progressively rougher pattern. As the crack propagates, a population of secondary cracks is generated as a result of the high local stress at the vicinity of the primary crack (either due to the presence of secondary defects or to the important local triaxial state of stress near the main crack tip [?]. The subsequent propagation of these secondary cracks leads to the parabolas observed on the micrographs B and mostly C of Fig.9.a, as also reported by Fiedler et al. [Fiedler et al., 2001] for uniaxial tension. The final region corresponds to the abrupt fracture of the specimen leading to a much rougher surface without any regular pattern.

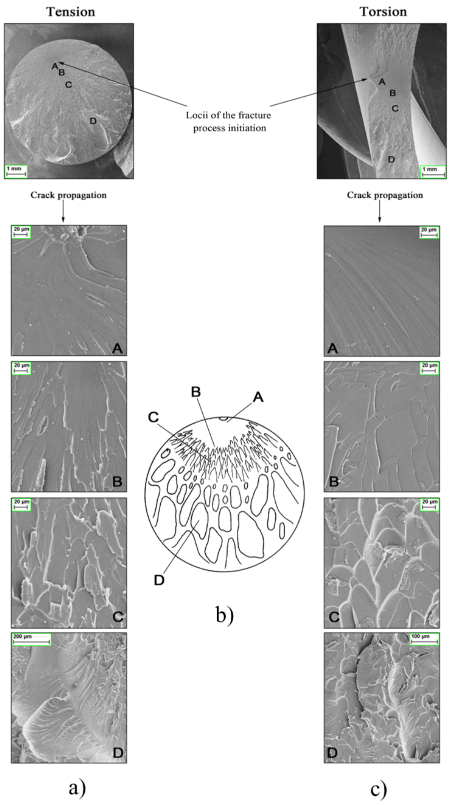

Figure 9: Detailed fracture surface analysis for tension (a) and torsion (c) test specimens. The schematic (b) is taken from [?] CHECK REF if not HULL.

The torsion specimens also failed in a brittle manner before any shear banding process, with fracture surfaces oriented at 45° with respect to the specimen longitudinal axis (see Fig.10.a), suggesting a failure mode dominated by the maximum principal stress value and orientation, confirming previous observations made by Fiedler et al. [Fiedler et al., 2001]. The evolution of the pattern observed on the fracture surfaces of the torsion specimens is illustrated in Fig.9.c. The features of the fracture surface for torsion are similar to those observed for tension, supporting the idea of a fracture scenario in torsion led by principal stresses. Note, however, that next to the brittle failure associated to normal principal stresses at 45° orientation, Fig.10.b suggests a deflection of the fracture path along maximum shear directions, after significant plastic deformation. The simultaneous presence of zones with brittle fracture related patterns and zones involving important plastic deformation in shear was also reported by Fiedler et al. [Fiedler et al., 2001]. Fig.11 shows two typical damage scenarios of a specimen loaded in uniaxial compression. The scenario

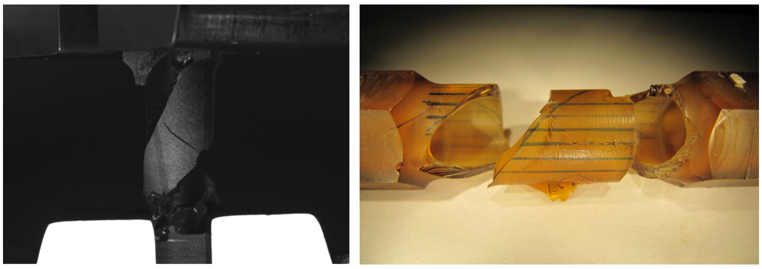

a) b)

Figure 10: a) Hollow tubular specimens loaded in torsion mostly fail along helicodal surfaces perpendicular to the MPS direction, i.e. oriented at +/-45° wrt to the specimen axis; b) crack deviation along maximum shear planes is also observed.

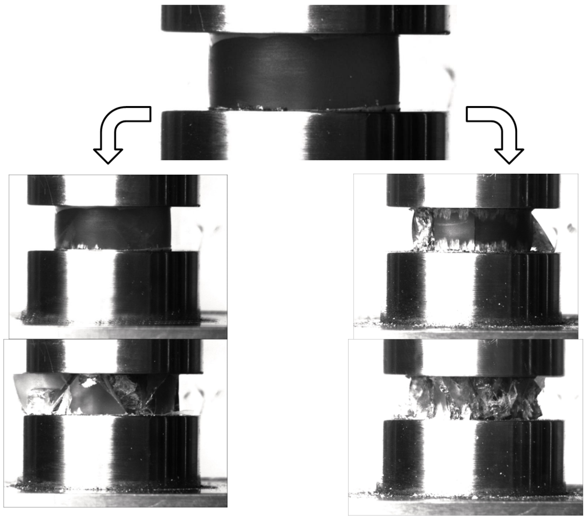

a) b)

Figure 11: Two different failure scenarios in compression specimen coming from the same batch of bulk resin (same testing temperature and constant strain rate): a) apparently dominated by maximum shear stress and b) apparently dominated by the presence of positive MPS.

depicted in Fig.11.a shows only a limited accumulation of cracks at the contact zone between the specimen and the platens until the very last instants of deformation. Failure mainly occurs along planes oriented at 45° with respect to the loading direction, suggesting a shear dominated failure mode, causing a sudden failure with a limited number of fragments. The scenario shown in Fig.11.b is more frequent. At moderate plastic strains, several cracks initiate and propagate in the contact zone, then coalesce with subsequent radial and hoop cracks leading to the formation of a diabolo-shaped chunk, as observed for other brittle materials such as concrete. However, these cracks do not directly lead to the final failure of the specimen. Hence the final failure of the specimen seems to result from a combination of shear-localization and brittle fracture. The specimen failure is, as in the case of tensile and torsion tests, very sudden with the production of a large number of small fragments. Fig.12 shows the two main types of fragments observed

a) b)

Figure 12: Uniaxial compression: fragments after failure: a) typical conical fragment with rough fracture surface, b) typical other fragment with essentially mirror-like fracture surfaces.

after failure of the specimen. Fig.12 shows the typical cones with rough fracture surfaces, which suggest at least a fraction of shear dominated failure. Fig.12 shows an example of fragment with mirror-like surfaces, which is the result of brittle failure perpendicular to a positive MPS. It is not clear whether one mode is more dominant than the other, and which one starts first and possibly triggers the other. Specimens with fewer cracks initiated during loading provide larger but fewer cones, while specimens exhibiting a large number of hoop and radial cracks provide a large number of smaller cones among the numerous fragments. The difference in roughness of

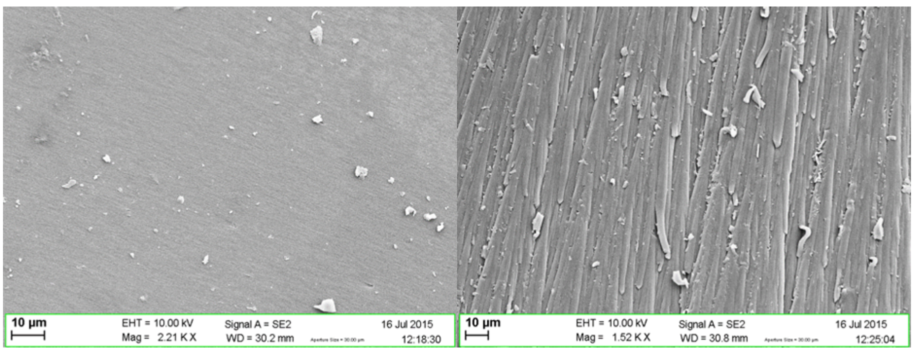

a) b)

Figure 13: Fracture surfaces after failure compression specimen examined by scanning electron microscopy: a) mirror-like fracture surface due to brittle failure, b) morphology observed on the fracture surface of the conical fragments, in line with the observations by Hobbiebruken et al. [ref].

the fracture surfaces already visible in Fig.12 is confirmed by SEM observation in Fig.13. Again, as illustrated on Fig.13.a, the truly mirror-like surfaces, showing the absence of any topological feature, clearly results from positive maximum principal stress dominated brittle failure. Characteristic features of a brittle fracture process such as parabolas, textured microflow and river lines are also occasionally encountered on these surfaces. Conversely, the rough fracture surface observed on the cones along maximum shear direction (see Fig.13.b) exhibits a triangular and rhombic morphology. While Fiedler et al. [Fiedler et al., 2001] explained the appearance of this typical morphology by the same mechanism as the one forming the parabolas in tension (nucleation of secondary cracks at defect sites), the 45° orientation of the fracture surface suggests that these rougher surfaces are instead the result of a shear-dominated failure. SEM micrographs of the fracture surfaces of a complete cone fragment provide additional hints on the evolution of the actual fracture process. The evolution of the fracture surface pattern along a single cone is represented in Fig.14. A closer look at the tips of the cones shows that most of the time there are several small cones initiated in a very confined area, see micrograph A of Fig.14. Smaller cones seem to merge into larger ones across the transition to a rougher fracture surface. The fracture pattern at the tip of the cones suggests that the cones may be initiated because of local high values of MPS. Indeed, the fracture surfaces right after the tips of the cones show a very smooth pattern (micrograph A of Fig.14), followed by river lines (see micrograph A and B of Fig.14), which is typical of a Mode I brittle fracture initiation followed by a mixed mode I/III propagation [**??**]. The subsequent development of the cones gives rise to rougher surfaces, as observed on the SEM micrographs C and D of Fig.14, eventually leading to the triangular and rhombic pattern already shown on Fig.13.

As a conclusion, the initiation of the final failure of the RTM6 is most probably due to positive MPS, as in the case of tension and torsion. The propagation of these initiated cracks can be controlled by the local MPS (longitudinal failure) or by shear stresses when meeting the zones of maximum shear stress (plane at 45° with respect to the loading direction).

4.3. Note on the sensitivity of uniaxial compression results to friction

Uniaxial compression tests are known to be sensitive to friction [Fiedler et al., 2001; Gearing and Anand, 2004; Gerlach et al., 2008; Liang and Liechti, 1996]. Friction between the specimen and the platens constraints the lateral movement of the sample, creates a heterogeneous state of stress, which departs from the uniform uniaxial target and can promote or delay the deformation and failure mechanisms. The most visible result of excessive friction between the specimen and the platens is the so-called barreling effect, illustrated in Fig.15. Fig.15.a shows a cylindrical sample tested in compression with a PTFE film used as solid lubricant: the specimen lateral edges are almost perfectly straight, proving that friction could be minimized; on the contrary, the specimen in Fig.15.b was loaded without any lubricant, and exhibits rounded edges. A map of hydrostatic stress computed using the finite element method and the constitutive model developed in the next sections is superimposed on Fig.15.b, it reveals large gradients and proves that uniaxial compression tests with significant friction cannot be considered as appropriate to identify the constitutive properties of polymers without the help of complex inverse analysis procedures. Similar detailed stress analyses of the barreling effect are reported in [Gearing and Anand, 2004]. Hence, when post-processed with the assumptions of plastic incompressibility and pure uniaxial stress, the constraining effect of friction provides stress-strain curves which actually erroneously suggest a material that exhibits a stronger apparent behavior than it really is, possibly missing the softening response. Fig.15.c shows the effect of friction on the apparent compressive behavior of the resin: for similar specimen dimensions, friction provides higher estimates of the peak yield and lower yield stresses. Moreover, theoretically, in the absence of friction, the aspect ratio of

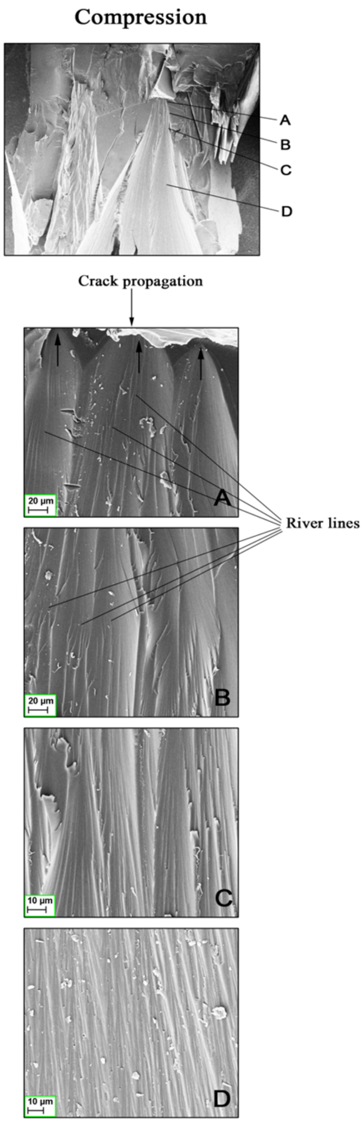

Figure 14: Detailed fracture surface analysis along a conical fragment in a failed compression specimen, from the tip (A) to the basis (D).

the specimen should have no effect on the measured stress-strain curve; on the contrary, with friction, increasing the diameter to height ratio leads to an apparently even stronger material.

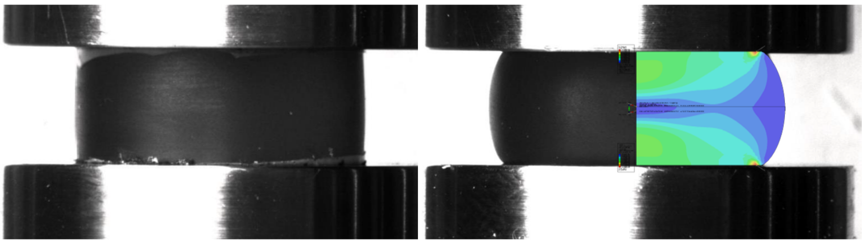

a) b)

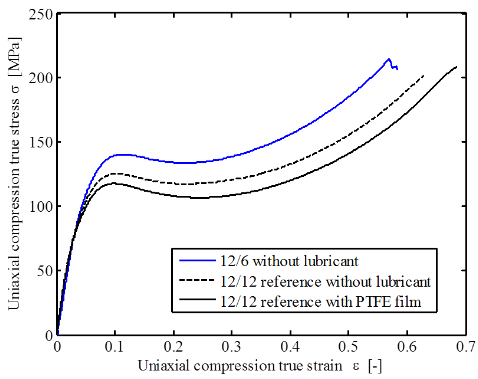

c)

Figure 15: Sensitivity of the compression test to friction between the sample and the platens: a) profile of the specimen at large deformation with solid lubricant (PTFE film), b) typical barrel-like profile of the specimen at large deformation without lubricant, the color map shows a distribution of hydrostatic pressure computed using the finite element method, c) apparent true stress-strain curves computed from the measured load displacement data with and without solid lubricant for a shape ratio of 12/12, and without lubricant for a 12/6 shape ratio.

5. Constitutive modeling

5.1. Selection of the constitutive model

The constitutive model was selected in order to be directly applicable with the standard distribution of the general purpose finite element software Abaqus [V6.12], without the need for coding a user defined material subroutine, favouring the application of the identified model in current engineering practice. Nevertheless, the ingredients of the model are chosen so that they can be directly compared or assessed towards more advanced finite strain elastic-viscoplastic models of the literature [Boyce et al., 1988; Poulain et al., 2014; Tervoort et al., 1996]. The behavior of the material is assumed to be elastic-plastic with rate and temperature dependences taken into account through the hardening law. The dependence of the hardening behavior on the strain rate and temperature is given explicitely to Abaqus, which makes the model useful for simulating loading rate and temperature effects in the frame of quasi-static simulations (strain-rate sensitivity comes the sepcification of a characteristic simulation time or loading history). In its present formulation, the model is thus not intended for use in the simulation of creep or relaxation. The selected yield criterion follows a linear Drucker-Prager [**??**] model, which is a pressure-modifed Von Mises yield surface. Isotropic hardening is assumed. An original hardening function incorporating pre-peak yield non-linearity, softening and re-hardening is developed. Strain-rate and temperature dependences of the true stress-strain curve are introduced via the coefficients of the hardening function.

5.2. Yield Criterion

The seminal linear Drucker-Prager yield criterion writes:

$$F = \sigma_e + \frac{\sigma_{mm}}{3} tan\,(\beta) - \left(1 - \frac{tan\,(\beta)}{3}\right)\sigma_c = 0 \tag{2}$$

where σ_e is the Von Mises effective stress, σ_{mm} is the trace of the stress tensor, σ_c is the yield stress in compression. The term β is the friction angle, defined as

$$tan\,(\beta) = \frac{3 - 3r}{1 + r} \tag{3}$$

with the so-called instantaneous uniaxial stress ratio'

$$r = \left|\frac{\sigma_c}{\sigma_p}\right| \tag{4}$$

where σ_t and σ_c are the true stress in uniaxial tension and uniaxial compression, respectively, at an arbitrary uniaxial plastic deformation p. In the linear Drucker-Prager model implemented in Abaqus, no dependence of the hardening behavior on the stress-state is allowed. Hence the hardening behavior is taken from uniaxial compression tests. Although some strain rate and/or temperature dependence of the friction angle cannot be excluded, they are not taken into account in the model.

5.3. Flow Rule

Beside the yield surface, a flow rule is selected based on the flow potential G defined as

$$G = \sigma_e + \frac{\sigma_{mm}}{3} tan\,(\varphi) \tag{5}$$

where φ is the so-called' dilation angle in the (σ_e,$-\frac{\sigma_{mm}}{3}$) plane. When , the incremental plastic strain vector is normal to the yield surface in the (σ_e,$-\frac{\sigma_{mm}}{3}$) plane and the plastic flow is associated with and derives from the yield criterion. When φ is different from β the flow is non-associated. When $\varphi = 0$, then plastic incompressibility is assumed. The non-associated flow rule can cause some convergence issues of the host finite element software when dealing with heterogeneous stress states. The dilation angle at a given plastic strain p is computed as

$$tan\,(\varphi) = -\frac{3\left(1 - 2\nu_p^c\right)}{2\left(1 + \nu_p^c\right)} \tag{6}$$

where ν_p^c is the plastic Poisson' coefficient measured in compression given by $\nu_p^c = \frac{p_r^c}{p_z^c}$ with p_r^c and p_z^c the radial and axial plastic strains under uniaxial compression. The plastic strain tensor is given by

$$p_{ij} = \varepsilon_{ij} - S_{ijkl}\sigma_{kl} \tag{7}$$

where ε_{ij} is the strain tensor, σ_{kl} is the Cauchy stress tensor, S_{ijkl} is the elastic compliance tensor. Although some strain rate and/or temperature dependence of the dilation angle cannot be excluded, they are not taken into account in the model.

5.4. *Elastic behaviour*

The resin is isotropic with Young's modulus E and Poisson ratio ν. For the sake of simplicity, the Poisson ratio is taken as rate and temperature insensitive. The asymmetry of Young's modulus between tension and compression is neglected and, as a first approximation, the experimental compression modulus is used. The compression modulus is assumed to take the following form:

$$E\left(T, ln(\dot{\varepsilon}\right) = \bar{E}(293)e^{\beta_T(T-293)} + k_\varepsilon\left(ln(\dot{\varepsilon}) - c_\varepsilon\right) \tag{8}$$

where $\bar{E}(293)$ is the compression modulus averaged over all strain rates at room temperature, c_ε is the average of the logarithms of all the tested true strain rates, β_T and k_ε are fitting parameters. The identified strain-rate dependence of the Young's modulus should hold up to strain rates of $100s^{-1}$, according to [Gerlach et al., 2008]. In most quasi-static loading situations, the dependence on strain-rate could even be neglected, taking $k_\varepsilon = 0$.

5.5. *Hardening behaviour*

The strain hardening is assumed not to depend on the stress triaxiality, which can be admitted for small to moderate strains; however, in general, the re-hardening part (stage IV in Fig.1) can be highly sensitive to the hydrostatic stress. Poulain et al. [Poulain et al., 2014] show that the hardening behaviour of a moderately crosslinked epoxy is different in tension and compression on the whole range of strain. The dependence on pressure of the element analogous to entropic resistance is thus not accounted for in the model. The hardening lwas is described by a sum of three main contributions: the pre-peak hardening behaviour ($\sigma_{Y02\%} + \sigma_A$) related with main chain segmental motion activation, the softening part σ_B coming from shear-transformation, localization combined with free volume rearrangement and then the re-hardening σ_C often referred to as the 'entropic spring' contribution. This approach, illustrated in Fig.16, is inspired by the work of Haward and Tackray [Haward and Thackray, 1968]. The present formulation relies

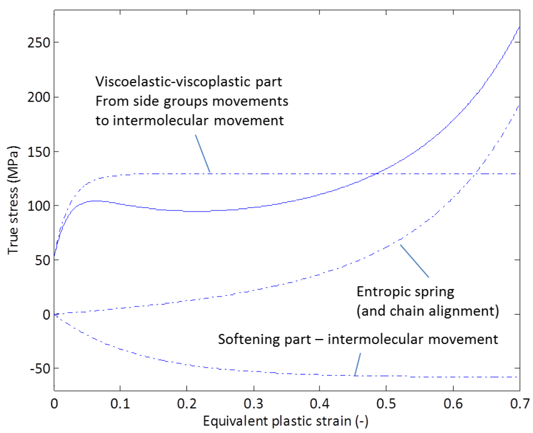

Figure 16: Decomposition of the hardening curve into three main contributions: ($\sigma_{Y02\%} + \sigma_A$), σ_B and σ_C.

on the commonly accepted understanding of the molecular motion of entangled or cross-linked glassy polymers during straining. Below the glass transition temperature, in order to achieve large inelastic strain, the polymer has to overcome two main types of physical-mechanical resistance: the intermolecular resistance ($\sigma_{Y02\%} + \sigma_A + \sigma_B$) and the term analogous to entropic resistance $\sigma_{C_{11}}$. At low strains, the polymer has to be loaded above the yield stress $\sigma_{Y02\%}$ (and with an appropriate stress triaxiality) in order to exceed the activation energy for segmental rotation. The contribution of this mechanism to the hardening of the polymer is denoted σ_A and has the following expression:

$$\sigma_A = \sigma_{A0}\left(1 - e^{-r_A p}\right) \tag{9}$$

where σ_{A0} is the targeted plateau overstress and r_A is a fitting parameter driving the hardening rate. The contribution of softening to the hardening of the polymer is denoted σ_B and writes:

$$\sigma_B = \sigma_{B0}\left(1 - e^{-r_B p}\right) \tag{10}$$

where σ_{B0} is the targeted plateau yield drop and r_B is a fitting parameter driving the softening rate. At larger strains, the latest contribution is analogous to the entropic resistance due to the alignment of the molecular network. This contribution is borrowed from the Arruda & Boyce 8-chain model of rubber elasticity [**?**]:

$$\sigma_{\mathbf{C}} = \frac{C_R}{3}\frac{\sqrt{N}}{\lambda_p}\mathcal{L}^{-1}\left(\frac{\lambda_p}{\sqrt{N}}\right) dev(\mathbf{B}) \tag{11}$$

where C_R is the hardening modulus (C_R is the rubbery modulus for material in the rubbery state), $\sqrt{N}$ the limiting chain extensibility, $\mathbf{B} = \mathbf{F}\mathbf{F}^{\mathbf{T}}$ is the left Cauchy-Green tensor and $dev(\mathbf{B})$ its deviator, with $\mathbf{F}$ the plastic deformation gradient (assuming plastic incompressibility)

$$\mathbf{F} = \begin{pmatrix} e^{p_{11}} & 0 & 0 \\ 0 & e^{p_{22}} & 0 \\ 0 & 0 & e^{p_{33}} \end{pmatrix} = \begin{pmatrix} e^{p} & 0 & 0 \\ 0 & e^{-0.5p} & 0 \\ 0 & 0 & e^{-0.5p} \end{pmatrix} \tag{12}$$

The term λ_p is the stretch on a chain of the 8-chain network defined as

$$\lambda_p = \sqrt{\frac{B_{mm}}{3}}. \tag{13}$$

The symbol $\mathcal{L}^{-1}$ represents the inverse Langevin function, which is here approximated by the explicit function

$$\mathcal{L}^{-1}(x) = \frac{9 - 3x^2}{1 - x^2} \tag{14}$$

Other expressions for the re-hardening could be assumed, considering for instance a Neo-Hookean behaviour, a 3-chain or 8-chain model or the approximated full-chain model by Wu and Van der Giessen [**?**]. Note that entropic springs such as the 8-chain model detailed in the expression of $\sigma_{\mathbf{C}}$ imply the existence of transverse stresses that should be iteratively removed by applying an appropriate transverse strain in order to recover pure uniaxial conditions; the present model overlooks this effect by taking into account the axial component of $\sigma_{\mathbf{C}}$ only. First, the impact of neglecting the transverse stresses brought by the entropic spring is that the identified parameters will be slightly different. Second, considering the spring as a simple hardening function relating the effective stress and the equivalent plastic strain cancels the multi-axial contribution and inherent pressure-sensitivity. The yield stress of the resin can then be expressed as

$$\sigma = \sigma_{Y02\%} + \sigma_{A0}\left(1 - e^{-r_A p}\right) + \sigma_{B0}\left(1 - e^{-r_B p}\right) + \sigma_{C_{11}} \tag{15}$$

Variable	Parameters
Modulus	β_T, k_ε, $\bar{E}(293)$, c_ε
Poisson ratio	ν
Stress ratio	r
Plastic Poisson ratio	ν_p^c
Activation volumes	Ω_{A_U}, $\Omega_{A_{Y02\%}}$, $\Omega_{A_{A0}}$
Activation enthalpies	ΔG_U, $\Delta G_{Y02\%}$, ΔG_{A0}
Reference transformation rates	$\dot{p}_{0_U}$, $\dot{p}_{0_{Y02\%}}$, $\dot{p}_{0_{A0}}$
Yield drop coefficient	k
Hardening kinetics coefficients	$r_{A,a}$, $r_{A,b}$, n_A
Softening kinetics coefficients	$r_{B,a}$, $r_{B,b}$, n_B
Rubbery modulus	C_R
Efficient chain segments	A_h, B_h, E_h, $N(293)$

Table 2: List of the parameters of the constitutive model

where $\sigma_{C_{11}}$ is the axial component of the re-hardening stress. Because of the underlying thermally and stress activated deformation mechanisms, the strain-rate and temperature dependence of the stress parameters $\sigma_{Y02\%}$ and σ_{A0} is assumed to follow the Eyrings equation, i.e.

$$\sigma_i = \frac{k_B T}{\Omega_{A_i}} \left(ln(\dot{p}) - ln(\dot{p}_0)\right) + \frac{\Delta G}{N_A \Omega_{A_i}} \tag{16}$$

with $i = Y02\%$ or $i = A0$; N_A is the Avogadro number. Inspired by the work of [Boyce et al., 1988] where the saturation stress is taken as a constant fraction of the so-called athermal shear strength, the strain rate and temperature dependence of σ_{B0} is introduced through $\sigma_{B0} = -k\sigma_U$ where k is a strain-rate and temperature insensitive fitting parameter named yield drop coefficient while σ_U is the strain-rate and temperature dependent peak yield stress, which also obeys Eyrings equation. The parameters r_A and r_B governing the pre-peak hardening rate and the softening rate are taken as

$$r_A = r_{A,a} T^{n_A} + r_{A,b} \tag{17}$$

and

$$r_B = r_{B,a} T^{n_B} + r_{B,b}. \tag{18}$$

In line with the approach of [?], C_R appearing in equation 14 is assumed independent of strain rate and temperature. Then $\sqrt{N}$ is taken independent of strain-rate while its sensitivity to temperature is expressed as

$$N(T) = \frac{n(293)N(293)}{B_h + A_h\left(1 - e^{-\frac{E_h}{k_B T}}\right)} \tag{19}$$

where $n(T)$ is the chain density at temperature T, E_h is the thermal dissociation energy and A_h and B_h are fitting parameters. This last expression expresses the fact that the number of efficient rigid links per chain $n(T)N(T)$ remains constant whatever the temperature. Alternatively, for materials below the glass transition temperature, Rottler [?] indicates that the hardening modulus C_R should depend linearly on the lower yield stress (having by consequence the same strain-rate and temperature sensitivities) and on the hydrostatic pressure.

β_T $[K^{-1}]$	k_ε $[MPa \cdot s]$	$\bar{E}(293)$ $[MPa]$	c_ε $[s^{-1}]$	ν $[-]$	r $[-]$	$\nu_p^c(p = 0.03)$ $[-]$
-0.00261	30.64	2587	-5.86	0.34	0.855	0.5
Ω_{A_U} $[J/mol]$	$\Omega_{A_{Y02\%}}$ $[J/mol]$	$\Omega_{A_{A0}}$ $[J/mol]$	ΔG_U $[s^{-1}]$	$\Delta G_{Y02\%}$ $[s^{-1}]$	ΔG_{A0} $[s^{-1}]$	$\dot{p}_{0_U}$ $[mm^3]$
$2.86 \cdot 10^5$	$2.06 \cdot 10^5$	$4.76 \cdot 10^5$	$2.83 \cdot 10^{23}$	$3.04 \cdot 10^7$	$8.79 \cdot 10^{49}$	$1.09 \cdot 10^{-18}$
$\dot{p}_{0_{Y02\%}}$ $[mm^3]$	$\dot{p}_{0_{A0}}$ $[mm^3]$	k $[MPa]$	$r_{A,a}$ $[-]$	$r_{A,b}$ $[-]$	n_A $[J/mol]$	$r_{B,a}$ $[-]$
$2.31 \cdot 10^{-18}$	$2.43 \cdot 10^{-18}$	26.6	$9.52 \cdot 10^{35}$	$11 \cdot 10^{31}$	8	1.87
$r_{B,b}$ $[-]$	n_B $[K^{-1}]$	C_R $[-]$	A_h $[-]$	B_h $[K^{-1}]$	E_h $[-]$	$N(293)$ $[-]$
0.954	$1.023 \cdot 10^{-10}$	35.88	4.63	$3.4 \cdot 10^{-20}$	2.15	7.54

Table 3: List of the parameters of the constitutive model

5.6. Parameters identification

Table 5.5 summarizes the parameters that must be identified. Some parameters can be directly identified from the experimental results, while others are identified through an inverse procedure of global fitting of the stress strain curves. The minimum set of experiments must involve four compression tests, e.g. two tests at different constant true strain rates and room temperature, and two tests at different temperatures, whatever the selected strain rate and one tensile test at room temperature and at a constant true strain rate (for which a RT compression test is also available). The identification of the model parameters is made through a two-step procedure:

- Several model parameters (13) can be identified directly against the experimental results: the modulus parameters β_T, k_ε, $\bar{E}(293)$, c_ε, the Poisson ratio ν, the stress ratio r, the plastic Poisson ratio ν_p^c (at room temperature, at a true plastic strain of 3%), the stress parameters $\sigma_{Y02\%}$ and σ_U (activation volumes, enthalpies and reference transformation rates that appear in Eyrings equation 16).
- The remaining model parameters (15) are identified by minimizing the distance between the predicted compression true stress-true plastic strain curves and the remarkable experimental couples shown in Fig. 1. Additionally the slope of the stress strain curve should be zero at the peak yield and lower yield. A gradient based optimizer provided in Matlab [16] is used for that purpose.

Table 3 shows the values identified for the parameters of the constitutive model. The identified activation volumes are in the same range as those reported in [Gómez-del Río and Rodríguez, 2012] for a DGEBA epoxy resin. The main parameters of the re-hardening part (C_R, N) are also comparable with values reported in the literature for other glassy polymers ([Poulain et al., 2014; **?**]). The true compression stress - true plastic strain curves resulting from the identification procedure are shown in Fig.17.b, with representative experimental results reproduced in Fig.17.a for the sake of comparison. A good agreement is found in terms of capability to reproduce the hardening behavior in the studied range of strain rates and temperature. Fig.17.c shows the behavior predicted in tension, obtained by multiplying the hardening curve identified in compression (for the same temperature and strain rate conditions) by the stress ratio identified at a 3% plastic strain.

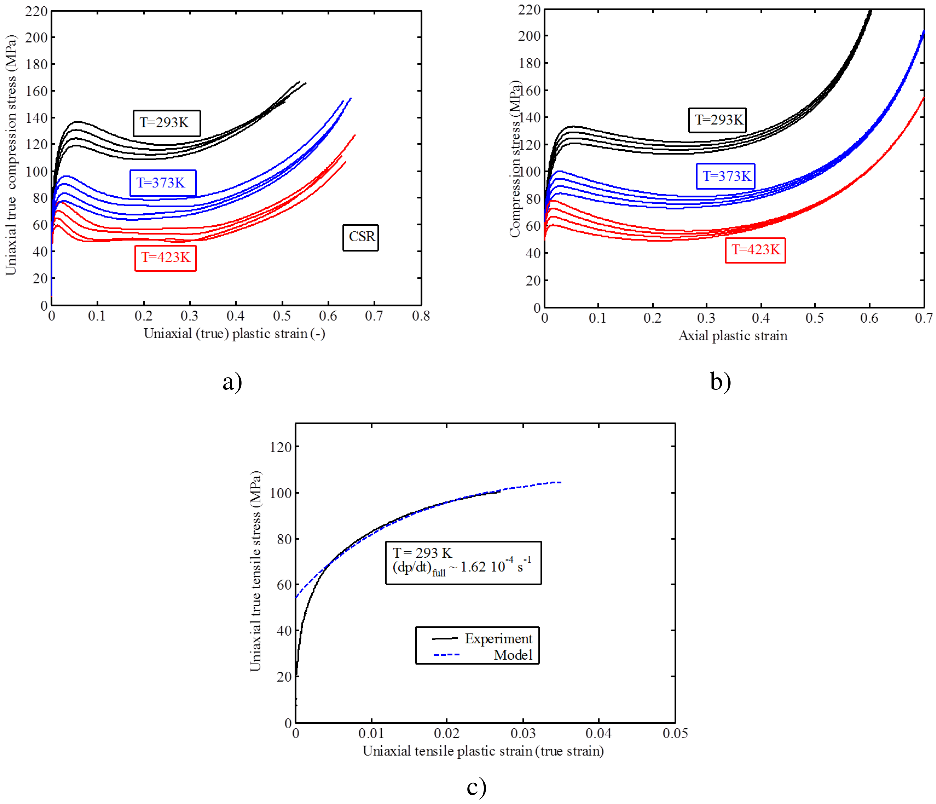

Figure 17: a) Experimental uniaxial compression curves obtained with constant strain rate tests, b) predicted uniaxial compression curves using the hardening law identification procedure, c) behavior predicted in tension, obtained by multiplying the hardening curve identified in compression (for the same temperature and strain rate conditions) by the stress ratio identified at a 3% true plastic strain.

5.7. Constitutive model as implemented in Abaqus

First, for what concerns the linear elastic behavior, the asymmetry of elastic modulus is neglected, the dependence of the modulus on the strain-rate is not taken into account and the Poisson ratio is assumed constant. Therefore, tabulated pairs of elastic modulus and temperature are provided to Abaqus. Second, the linear Drucker-Prager model is selected, and the friction and dilation angles identified in the previous section are specified. The hardening behavior is introduced in Abaqus by providing tables of pairs of Von Mises stress and equivalent plastic strains (i.e. the hardening curves in compression) at different strain-rates and temperatures. In this context, Abaqus requires a virtual zero strain rate hardening response, which can for instance be arbitrarily taken as the curve predicted by the constitutive model at a plastic strain rate of $10^{-12}s^{-1}$. Abaqus interpolates between the curves provided by the user, and extrapolates at higher strain rates, CHECK CHECK CHECK by using to a simple power-law dependence of the stress on the strain-rate. Other parameters are left to the default value. The model is thus readily available in Abaqus. Due to the softening of the resin, in certain circumstances (e.g. large gradients, or very local stress concentration), the standard quasi-static non-linear finite element solver could encounter major convergence issues. In this case, switching to arc length methods helps. However in several occasions, the user will have to change to fully explicit simulations, with appropriate mass scaling and viscosity, to reach a consistent, converged solution.

5.8. Validation of the constitutive model

The predictive capability of the identified model is assessed against experimental results which were not used for parameters identification:

- the hardening behavior in shear at room temperature i.e. $293K$, obtained by torsion testing of hollow cylindrical specimen at a rotation rate of $7^{\circ}/min$. Fig.18.a shows the curves identified in compression and tension, and the prediction of the model for the case of torsion. Despite minor differences of experimental plastic strain rates, the response predicted in shear (black curve) is equidistant from the compression and tension curves due to the hypothesis of linear dependence of yielding on the hydrostatic pressure, and falls close to the curve representative of shear loading.

- The hardening behavior in tension at temperatures of $373K$ and $423K$ and a constant crosshead displacement rate of $1mm/min$; Fig.18.b shows the predictions of the model in terms of the tensile behavior at higher temperatures. The agreement is here not very good, as the stress ratio identified at room temperature seems to be temperature dependent. Hence, the tension-compression asymmetry is underestimated at $373K$ and $423K$. The tension-compression asymmetry being attributed to the different behavior of free volume under tensile and compressive stresses and the evolution of this free volume (movement, creation and annihilation) being thermally activated, it is reasonable to think that an additional temperature dependence of the stress ratio should be incorporated.

- The non-linear relationship between notch diameter reduction (striction) and the tensile load on the notch tensile tests conducted at a constant crosshead displacement rate of $1mm/min$, at room temperature, for three different notch radii. In this case, explicit simulations were performed using Abaqus v6.12 in order to properly account for the important heterogeneity of hydrostatic stress and strain-rate in the gauge length. Fig.18.c reveals a very good agreement between the FE results and the experimental data for the three notch radii.

- the compression true stress- true strain curves obtained at room temperature and a $1mm/min$ constant crosshead displacement rate with different conditions of friction with the platens. Chevalier et al. [**?**] have shown that a friction coefficient of 0.07 is necessary in order to perfectly reproduce the barreling profile using FE simulation with the model presented in this section. Fig.18.d shows that the FE simulation of the compression test without lubricant, for a similar diameter to height ratio (12/12), is remarkably close to the corresponding apparent experimental uniaxial true stress-true strain curve. Note that the discrepancies in the non-linear behavior could partly be attributed to batch to batch variability as the model was identified on another batch. Increasing the diameter to height ratio (e.g. here 12/6) makes the constraining effect of friction more prominent. Hence the friction coefficient must be increased to 0.2 in order to capture the experimental behavior. In this case, part of the error lies in the inability of the model to deal with larger stress gradients and another part in the too simplistic modeling of friction.

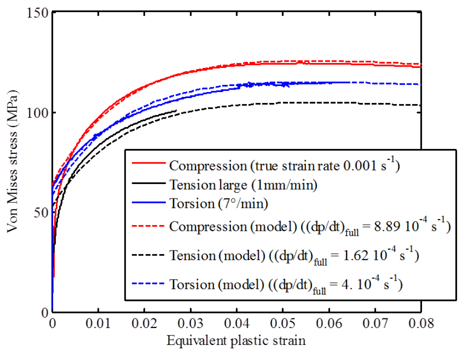

a)

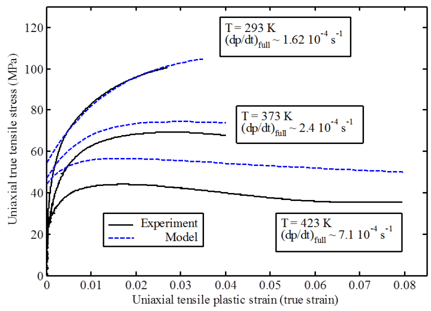

b)

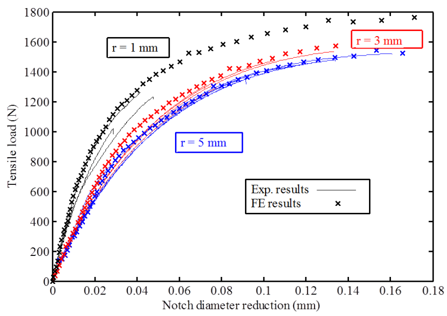

c)

Figure 18: Constitutive model assessment: a) Von Mises stress versus Equivalent plastic strain curves for uniaxial compression, tension and for torsion, predicted using the identified hardening law and the identified pressure dependence of yielding (linear Drucker-Prager); b) predicted temperature dependence of yielding under tensile loading, note the apparent dependence of pressure sensitivity on temperature; c) predicted load - notch striction curve for three different notch radii and a constant crosshead displacement rate of $1mm/min$; d) prediction of the apparent compression true stress true strain curves with and without solid lubricant, and for different cylinder diameter/height ratios.

6. Failure Criterion

6.1. Preamble

No detectable damage evolution is observed in RTM6. Despite significant non-linear deformation, there is no evidence of intrinsic progressive damage mechanisms such as void growth and coalescence observed for instance in ductile metals or blended polymer, or crazing which is commonly observed in thermoplastics. Hence, in section 4.2, no microstructural features or morphologies on the fracture surfaces could be associated with an intrinsic progressive damage mechanism or extensive plasticity. No progressive drop of the Youngs modulus is observed either, which could have been considered as an indirect proof of damage incurred in the specimen. Furthermore, Morelle [**?**] observed on the same resin a rapid saturation of the backstress upon unloading, which is another argument in favor of the idea of the absence of progressive damage. Hence, failure appears to be brittle in all circumstances (tension, notched-tension, torsion, compression) whatever the amount of plastic deformation. This is in-line with the researches reported in [Asp et al., 1996; Fiedler et al., 2001, 2005; Hobbiebrunken and Fiedler, 2007] which converge to the idea of a competition between shear-dominated yielding and brittle failure driven by a positive hydrostatic and/or MPS related with micro-cavitation and chain scission.

Therefore, failure has been addressed based on an un-coupled approach as a post-processing task, considering that fracture occurs when some combination of stress or strain reaches a critical value, and that cracking is catastrophic, with almost no post-failure (visco-) plastic dissipation.

6.2. Failure criteria

Four different criteria have been selected and assessed:

- FC I. In-line with the common understanding of brittle failure in highly-crosslinked epoxies, the first criterion considers that failure occurs when a pressure-modified maximum principal stress is reached (Eq. 20):

$$\sigma_{MAX} - a\sigma_H - b = 0 \tag{20}$$

  This criterion can be easily identified using the failure stress data in tension and compression.

- FC II. The second criterion is an hyperbolic criterion, similar in form to some crazing initiation criteria as reviewed in [Gearing and Anand, 2004]:

$$\sigma_e = \frac{a}{\sigma_H + b} + c \tag{21}$$

  This criterion is actually a pressure-modified critical distortional strain energy criterion. The three parameters must be identified using the failure stress data in tension, compression and torsion.

- FCIII. The third criterion is a pressure-modified maximum shear criterion, similar to a pressure-modified Tresca criterion, motivated by the occasional observation of a shear-dominated failure mode as observed in Fig.11.a:

$$|\sigma_{MAX} - \sigma_{MIN}| - a\sigma_H - b = 0 \tag{22}$$

  This criterion can be easily identified using the failure stress data in tension and compression

- FCIV. The fourth criterion is a triaxiality-dependent critical equivalent plastic strain at failure criterion, often used in the modeling of the ductile failure of metals:

$$p_e - ae^{-b\frac{\sigma_e}{\sigma_H}} - c = 0 \tag{23}$$

  The three parameters must be identified using the failure stress data in tension, compression and torsion.

Criterion	a	b	c
FCI	$1064[-]$	$66[MPa]$	-
FCII	$5352[MPa]$	$105.7[MPa]$	$63[MPa^2]$
FCIII	$-0.8824[-]$	$132[MPa]$	-
FCIV	$0.04042[-]$	$7.815[-]$	$0.02558[-]$

Table 4: Value of the parameters identified for the four failure criteria.

6.3. Parameters identification and validation

The parameters of the four failure criteria have been identified directly using the experimental failure stress data, see Table 6.3. Fig.19.a shows the variation of the fracture stress as a function

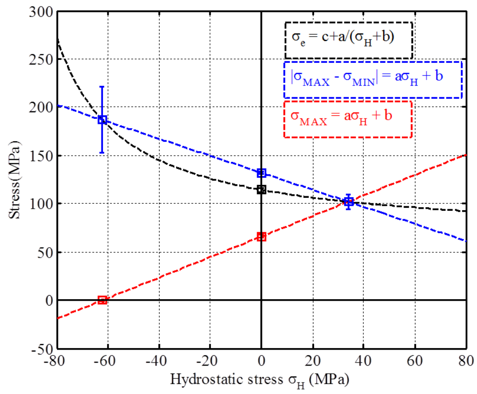

a)

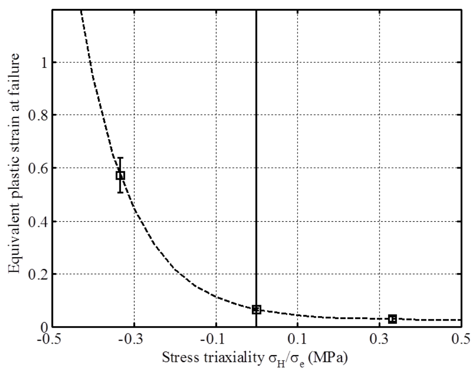

b)

Figure 19: a) Stress based failure criteria: pressure-dependent critical maximum principal stress (red) identified with the compression and tension data, pressure-dependent critical Von Mises stress (black) identified with the compression, tension and torsion data, pressure-dependent critical maximum shear stress (blue) identified with the compression and tension data; b) critical equivalent plastic strain at failure criteria (negative exponential) identified with the compression, tension and torsion data.

of the hydrostatic stress for the criteria FCI, FCII, and FCIII. FCI and FCIII can be assessed by comparison of the prediction of the failure stress in torsion with the experimental value, as the latter was not used for identification, showing excellent agreement. Fig.19.b shows the variation of criterion FCIV as a function of the stress triaxiality. The four failure criteria were used in combination with the constitutive model in FE simulations of the notched tensile tests in order to predict the maximum load and notch diameter reduction at failure. Fig.20.a shows that all but the pressure-modified MPS criterion (FCI) predict an increase of the maximum load at failure with an increasing notch radius. The pressure-modified maximum shear stress criterion (FCIII) significantly underestimates the various loads. Despite the fact that it does not reproduce the correct load evolution with notch radius, criterion FCI falls within the experimental variability for the 1 and 3*mm* notch radii. Besides, the triaxiality-dependent equivalent plastic strain at failure (FCIV) performs very well. All the models correctly predict the increase of notch diameter reduction with increasing notch radius, and it is again the triaxiality-dependent plastic strain at failure criterion FCIV which performs best. The pressure-modified MPS criterion performs also quite well. Criterion FCIV is readily introduced in Abaqus as Ductile fracture criterion.

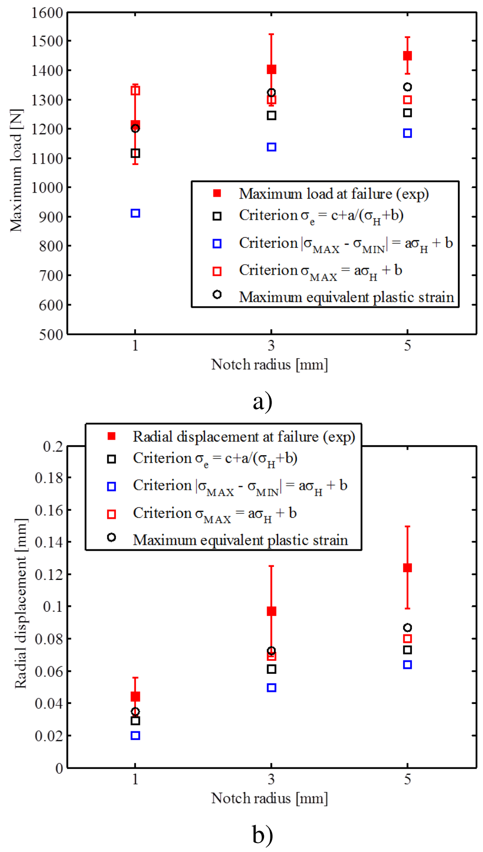

Figure 20: Model assessment (non-linear behavior and failure) against experimental results on notched tensile tests: a) experimental versus predicted failure load, b) experimental versus predicted radial displacement in the notch (local striction).

Pairs of equivalent plastic strain at failure and stress triaxiality must be provided, for different temperatures and strain-rates. In this case, the failure criterion was provided at a reference strain-rate of $10^{-3}s^{-1}$ and a temperature of $293K$, assuming first that failure is independent of strain-rate. This allows simulating crack initiation in deformed components.

7. Full model assessment - Iosipescu case study

The original intent of this paper is to build, identify, and assess a model that can be used in the framework of the multi-scale modeling of the deformation and failure of carbon-epoxy composites where highly heterogeneous stress and strain fields are encountered. However, before addressing this level of complexity, it is important, in terms of methodology, to first assess the model against a simpler configuration where field heterogeneity is moderate but with a clear contrast between zones with distinct shear-dominated and hydrostatic stress / maximum principal stress dominated conditions.
The test selected for validation comes from the ASTM5379 V-notched beam method standard, with set-up and sample illustrated in Fig.21.a. The V-notched beam method is in principle dedicated to the measurement of the shear properties of composite materials with continuous or short fibres. Hence, a good portion of the ligament between the V notches undergoes uniform shear stresses. However, as depicted in the stress triaxiality map right before failure in Fig.21.b (see description of the FE model below), although most of the deformed zone is shear-dominated (zone A), high tensile stresses are generated on the surface close to the notch roots (zone B), while compressive stresses are induced at the end of the contact zone with the load fixture (zone C). With an unreinforced isotropic material, this test is somehow critical as the non-linear behavior should be mostly determined by the response in shear between the notch roots, while failure should be triggered elsewhere. The V-notched beam specimens were produced with the processing and machining conditions described in section 2. A series of five tests were performed on a screw-driven universal Zwick-Roell testing machine with an external load cell of 250 [kN], at 293K and a crosshead displacement rate of $1mm/min$. The maximum and minimum principal strain were measured using back-to-back bi-directional strain gauges positioned between the notch roots at 45 with reference to the horizontal axis.
A two-dimensional explicit finite element model was set-up in Abaqus 6.12 to simulate the test, with a global mesh size of $0.5mm$, using linear triangular plane stress elements. A local size of $0.1mm$ was imposed at the notch roots. Frictionless contact was assumed. The constitutive model was introduced as explained in section 5.7. The failure criterion FCIV identified at RT and a strain rate of $10^{-3}s^{-1}$ in section 6.2 was introduced in Abaqus as explained in section 6.3. In addition to that, progressive failure analysis, using a smeared crack approach, was enabled by using the Damage Evolution feature of the Ductile failure criterion with an exponential softening law, given an arbitrary post-failure energy of $1mJ$, which leads to rapid failure when the criterion is met. Appropriate mass scaling was used in order to accelerate the simulations while not perturbing the solution. The model is assessed against experimental results as follows:

- The predicted and experimental load-displacement curves, maximum load and displacement at failure are compared (see Fig.22.a). Good agreement is found although the predicted load at failure falls below the error box.

- The predicted and experimental shear strain at the locus of the strain-gauge between the notch roots are compared (see Fig.22.b). Good agreement is found for what concerns the linear part of the measured shear strain, however, after the onset of plasticity, the prediction overestimates the experimental value by up to 20%.

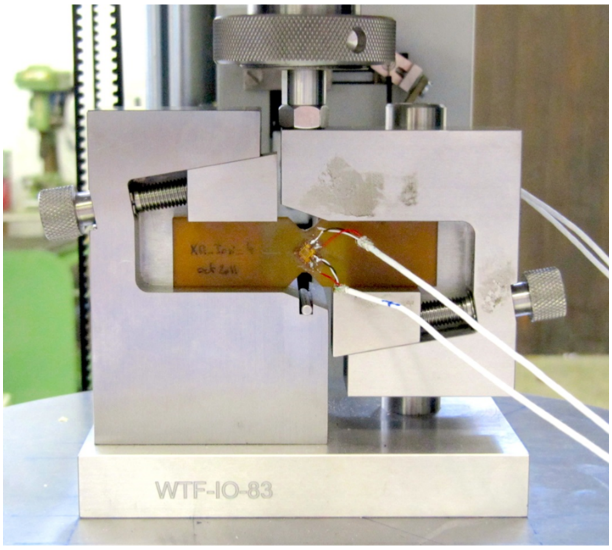

a)

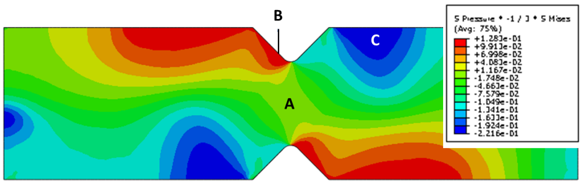

b)

Figure 21: a) The V-notch beam test sample instrumented with back-to-back bidirectional strain gauges, and load introduction fixture; b) Map of stress triaxiality on the V-notch specimen just before failure: zone A is the shear-dominated zone (triaxiality close to zero), zone B is dominated by tensile stresses and exhibits the maximum triaxiality (above 1.2), zone C is essentially compressive.

- The predicted and observed failure hierarchy and final crack path are compared (Fig.22.c). Excellent agreement is found, in-line with the failure mode observed by Hodgkinson in [**?**] for unreinforced brittle thermoset materials.

The explanation for the underestimation of the load at yielding and for the overestimation of the non-linearity is four-fold:

- Early plasticity is predicted in the simulation in the stress concentration areas located at the end of the contact zone between the load introduction rig and the sample (zone C in Fig.21.b). This stress concentration favours a root rotation of the shear dominated zone and lead to an overestimation of the specimen tangent compliance.

- The absence of friction in the simulations accelerates the onset of yielding and leads to a more compliant overall response. Hence adding friction between the load introduction rig and the sample in the simulation helps delaying the onset of yielding, but not sufficiently. Note that the experimental maximum and minimum principal strains measured by the strain gauge are slightly asymmetric (up to 10% of difference); according to the simulations, this asymmetry increases with increasing friction.

- Part of the discrepancy might be attributed to batch-to-batch variability which is known to be of up to 10% for what concerns the peak yield in compression.
- The constitutive model overestimates (either or both) the strain-rate sensitivity (note: the equivalent plastic strain rate in the simulation amounts from 0.0002 to $0.0008 s^{-1}$) and the pressure sensitivity of yielding of the material.

Finally, it is worth mentioning that fracture being driven by a positive MPS, a fracture surface similar to what was obtained in tensile and torsion specimen was expected. The detailed fracture surface analysis shown in Fig.23 confirms the different steps in terms of successive crack surface patterns, and shows again that the crack initiates in the zone where the maximum principal stress is critical.

8. Conclusion and future work

The elastic, viscoplastic and fracture of the RTM6 resin was characterized as a function of strain rate and temperature under various loading conditions involving uniaxial tension, notched tension, uniaxial compression, torsion and shear. When loaded in compression, the RTM6 was shown to behave like amorphous thermoplastics in the glassy state, with four expected distinct deformation stages up to large strains, and exhibiting e.g. similar dependences of the peak yield on temperature and strain-rates. Limited ductility was observed however for any other loading condition. Unlike thermoplastics though, brittle failure was always observed, and no progressive damage mechanism could be identified. Detailed fractography analysis provided insight into the competition between shear yielding and maximum principal stress driven brittle failure. A Drucker-Prager pressure-dependent constitutive model was built. A specific hardening law was developed with strain-rate and temperature dependent parameters, owing e.g. to Eyring's theory of transition of state or to the theory of rubber elasticity. The pressure-dependence and hardening law, as well as four different failure criteria were identified against the experimental results using a two-step procedure involving direct identification and reverse analysis. This identification procedure requires at most four uniaxial compression tests and one uniaxial tensile test. After thorough verification, the constitutive model and a plastic strain at failure criterion were readily introduced in the standard version of Abaqus. The model was successfully assessed against results of progressive failure in V-notched beam shear test in terms of overall load-displacement curve, local shear-strain / shear-stress and predicted failure path. Short-term perspectives involve

- The modeling of the deformation and failure of RTM-processed uni-directional composites loaded in transverse compression.
- The adaptation of finite strain elastic-viscoplastic constitutive models to capture unloading, fully reverse loading, creep, relaxation and recovery behaviour of the RTM6.

Acknowledgements

This work was funded by the Fond de la Recherche Scientifique through a FNRS doctoral fellowship (grant number XXXX). The authors are grateful to Maxime Melchior and Laurence Brassart for fruitful discussions. The authors thank Alban Maton for his precious help machining the numerous samples.

References

Anand, L., Ames, N.M., Srivastava, V., Chester, S.a., 2009. A thermo-mechanically coupled theory for large deformations of amorphous polymers. Part I: Formulation. International Journal of Plasticity 25, 1474–1494.

Anand, L., Gurtin, M.E., 2003. A theory of amorphous solids undergoing large deformations , with application to polymeric glasses. International Journal of Solids and Structures 40, 1465–1487.

Argon, A.S., 1973. A theory for the low-temperature plastic deformation of glassy polymers. Philosophical Magazine 28, 839–865.

Argon, A.S., Bessonov, M.I., 1977. Plastic Flow in Glassy Polymers. Polymer Engineering and Science 17, 174–182.

Asp, L.E., Berglund, L.a., Talreja, R., 1996. A criterion for crack initiation in glassy polymers subjected to a composite-like stress state. Composites Science and Technology 56, 1291–1301.

Boyce, M.C., Parks, D.M., Argon, A.S., 1988. Large inelastic deformation of glassy polymers. part I: rate dependent constitutive model. Mechanics of Materials 7, 15–33.

Canal, L.P., González, C., Segurado, J., LLorca, J., 2012. Intraply fracture of fiber-reinforced composites: Microscopic mechanisms and modeling. Composites Science and Technology 72, 1223–1232.

Dumont, D., 2013. Thermoplastic as carrier for delivering carbon nanotubes and layered clay in epoxy resin for composite applications. Phd thesis. Université catholique de Louvain.

Eyring, H., 1936. Viscosity, Plasticity, and Diffusion as Examples of Absolute Reaction Rates. The Journal of Chemical Physics 4, 283–291.

Fiedler, B., Hojo, M., Ochiai, S., Schulte, K., Ando, M., 2001. Failure behavior of an epoxy matrix under different kinds of static loading. Composites Science and Technology 61, 1615–1624.

Fiedler, B., Thomas, H., Schulte, K., 2005. Influence of stress state and temperature on the strength of epoxy resins, in: 15th International Conference on Composites Materials, Durban, South Africa. p. 6376.

Gearing, B.P., Anand, L., 2004. On modeling the deformation and fracture response of glassy polymers due to shear-yielding and crazing. International Journal of Solids and Structures 41, 3125–3150.

Gerlach, R., Siviour, C.R., Petrinic, N., Wiegand, J., 2008. Experimental characterisation and constitutive modelling of RTM-6 resin under impact loading. Polymer 49, 2728–2737.

Goldberg, R.K., Roberts, G.D., Gilat, A., 2003. Incorporation of mean stress effects into the micromechanical analysis of the high strain rate response of polymer matrix composites. Composites, Part B 34, 151–165.

Gómez-del Río, T., Rodríguez, J., 2012. Compression yielding of epoxy: Strain rate and temperature effect. Materials & Design 35, 369–373.

Govaert, L.E., Engels, T.A., Wendlandt, M., Tervoort, T.A., Suter, U.W., 2008. Does the Strain Hardening Modulus of Glassy Polymers Scale with the Flow Stress? Journal of Polymer Science Part B: Polymer Physics 46, 2475–2481. 0406218.

Govaert, L.E., Timmermans, P.H.M., Brekelmans, W.a.M., 2000. The Influence of Intrinsic Strain Softening on Strain Localization in Polycarbonate: Modeling and Experimental Validation. Journal of Engineering Materials and Technology 122, 177.

G'Sell, C., Gopez, a.J., 1985. Plastic banding in glassy polycarbonate under plane simple shear. Journal of Materials Science 20, 3462–3478.

Hasan, O.A., Boyce, M.C., 1995. A Constitutive Model for the Nonlinear Viscoelastic Viscoplastic Behavior of Glassy Polymers. Polymer Engineering & Science 35, 331.

Hasan, O.A., Boyce, M.C., Li, X.S., Berko, S., 1993. An investigation of the yield and postyield behavior and corresponding structure of poly(methyl methacrylate). Journal of Polymer Science Part B: Polymer Physics 31, 185–197.

Haward, R., Thackray, G., 1968. . Proc. Royal Society 302, 453.

Hobbiebrunken, T., Fiedler, B., 2007. Experimental determination of the true epoxy resin strength using micro-scaled specimens. Composites, Part A : applied science and manufacturing 38, 814–818.

Homer, E.R., Schuh, C.A., 2009. Mesoscale modeling of amorphous metals by shear transformation zone dynamics. Acta Materialia 57, 2823–2833.

Jatin, Sudarkodi, V., Basu, S., 2013. Investigations into the origins of plastic flow and strain hardening in amorphous glassy polymers. International Journal of Plasticity 56, 139–155.

Kiuna, N., Lawrence, C.J., Fontana, Q.P.V., Lee, P.D., Selerland, T., Spelt, P.D.M., 2002. A model for resin viscosity during cure in the resin transfer moulding process. Composites Part A: Applied Science and Manufacturing 33, 1497–1503.

Klompen, E.T.J., Engels, T.A.P., Govaert, L.E., Meijer, H.E.H., 2005. Modeling of the Postyield Response of Glassy Polymers : Influence of Thermomechanical History. Macromolecules 38, 6997–7008.

Liang, Y.M., Liechti, K.M., 1996. On the large deformation and localization behavior of an epoxy resin under multiaxial stress states. International Journal of Solids and Structures 33, 1479–1500.

Marano, C., Rink, M., 2001. Shear yielding threshold and viscoelasticity in an amorphous glassy polymer: a study on a styrene-acrylonitrile copolymer. Polymer 42, 2113–2119.

Meijer, H.E., Govaert, L.E., 2005. Mechanical performance of polymer systems: The relation between structure and properties. Progress in Polymer Science 30, 915–938.

Morelle, X.P., Bahrami, A., Lani, F., Melchior, M.a., Nysten, B., Bailly, C., Pardoen, T., 2014. Characterization and Modeling of the Time-Dependent Behavior of the Rtm6 Structural Epoxy Involving Recovery , Creep and Back Stress, in: 16th European Conference on Composite Materials, Sevilla, Spain.

Oleynik, E., 1989. Plastic deformation and mobility in glassy polymers, in: Pietralla, M., Pechhold, W. (Eds.), Relaxation in Polymers SE - 19. Steinkopff. volume 80 of *Progress in Colloid & Polymer Science*, pp. 140–150.

Poulain, X., Benzerga, a.A., Goldberg, R.K., 2014. Finite-strain elasto-viscoplastic behavior of an epoxy resin: Experiments and modeling in the glassy regime. International Journal of Plasticity 62, 138–161.

Poulain, X., Kohlman, L.W., Binienda, W., Roberts, G.D., Goldberg, R.K., Benzerga, a.a., 2013. Determination of the intrinsic behavior of polymers using digital image correlation combined with video-monitored testing. International Journal of Solids and Structures 50, 1869–1878.

Quinson, R., Perez, J., Rink, M., Pavan, A., 1996. Components of non-elastic deformation in amorphous glassy polymers. Journal of Materials Science 31, 4387–4394.

Ree, T., Eyring, H., 1955. Theory of non-Newtonian flow. I. Solid plastic system. Journal of Applied Physics 26, 793–800.

Senden, D., Van Dommelen, J., Govaert, L.E., 2010. Strain Hardening and Its Relation to Bauschinger Effects in Oriented Polymers. Journal of Polymer Science Part B: Polymer Physics 48, 1483–1494.

Sindt, O., Perez, J., Gerard, J.F., 1996. Molecular architecture-mechanical behaviour relationships in epoxy networks. Polymer 37, 2989–2997.

Struik, L.C.E., 1991. Some problems in the non-linear viscoelasticity of amorphous glassy polymers. Journal of Non-Crystalline Solids 133, 395–407.

Tervoort, T., Klompen, E.J., Govaert, L.E., 1996. A multi-mode approach to finite, three-dimensional, nonlinear viscoelastic behavior of polymer glasses. Journal of Rheology 40, 779.

Tervoort, T.A., Govaert, L.E., 1998. A Constitutive Equation for the Elasto-Viscoplastic Deformation of Glassy Polymers. Mechanics of Materials 1, 269–291.

V6.12, A., . General purpose finite element software.

Westbrook, K.K., Kao, P.H., Castro, F., Ding, Y., Jerry Qi, H., 2011. A 3D finite deformation constitutive model for amorphous shape memory polymers: A multi-branch modeling approach for nonequilibrium relaxation processes. Mechanics of Materials 43, 853–869.

Yamini, S., Young, R.J., 1980. The mechanical properties of epoxy resins - Part 1 : Mechanisms of plastic deformation. Journal of Materials Science 15, 1814–1822.

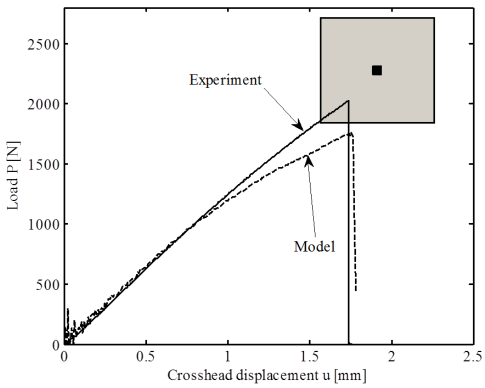

a)

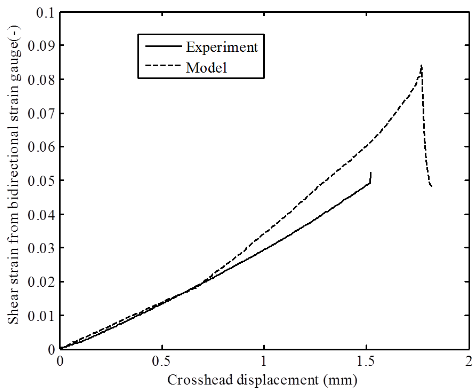

b)

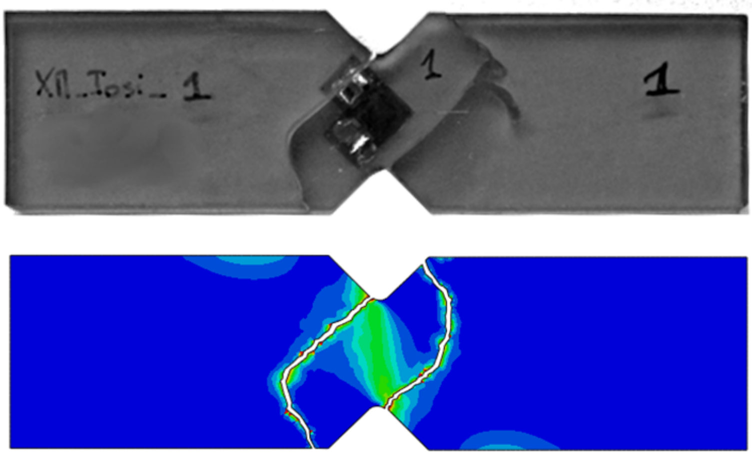

c)

Figure 22: a) Experimental representative load-displacement curve between the notch roots and predicted counterpart. The grey rectangle is the error box for the pair experimental load at failure - displacement at failure; b) Comparison of the shear strain measured experimentally between the notch roots (representative curve) and the computed shear strain averaged over the strain gauge area in the FE model; c) Comparison of the experimental (TOP) and predicted crack paths (BOTTOM). The bottom image shows a map of the value of the failure criterion, the elements which have failed have been deactivated and eventually constitute the crack path.

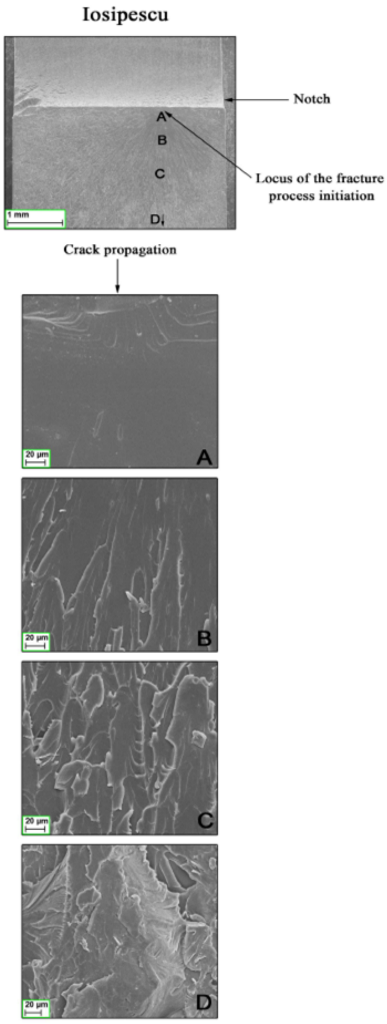

Figure 23: Detailed fracture surface analysis after failure of the V-notch beam specimen.